Constraints on the Formation of the Galactic Bulge from Na, Al, and Heavy Element Abundances in Plaut's Field

Christian I. Johnson[1,5], R. Michael Rich[1], Chiaki Kobayashi[2], and Jon P. Fulbright[3,4]

ABSTRACT

We report chemical abundances of Na, Al, Zr, La, Nd, and Eu for 39 red giant branch (RGB) stars and 23 potential inner disk red clump stars located in Plaut's low extinction window. We also measure lithium for a super Li–rich RGB star. The abundances were determined by spectrum synthesis of high resolution (R≈25,000), high signal–to–noise (S/N∼50–100 pixel^{-1}) spectra obtained with the Blanco 4m telescope and Hydra multifiber spectrograph. For the bulge RGB stars, we find a general increase in the [Na/Fe] and [Na/Al] ratios with increasing metallicity, and a similar decrease in [La/Fe] and [Nd/Fe]. Additionally, the [Al/Fe] and [Eu/Fe] abundance trends almost identically follow those of the α–elements, and the [Zr/Fe] ratios exhibit relatively little change with [Fe/H]. The consistently low [La/Eu] ratios of the RGB stars indicate that at least a majority of bulge stars formed rapidly ($\lesssim$1 Gyr) and before the main s–process could become a significant pollution source. In contrast, we find that the potential inner disk clump stars exhibit abundance patterns more similar to those of the thin and thick disks. Comparisons between the abundance trends at different bulge locations suggest that the inner and outer bulge formed on similar timescales. However, we find evidence of some abundance differences between the most metal–poor and metal–rich stars in various bulge fields. The data also indicate that the halo may have had a more significant impact on the outer bulge

[1]Department of Physics and Astronomy, UCLA, 430 Portola Plaza, Box 951547, Los Angeles, CA 90095-1547, USA; cijohnson@astro.ucla.edu; rmr@astro.ucla.edu

[2]Centre for Astrophysics Research, University of Hertfordshire, Hatfield AL10 9AB, UK; c.kobayashi@herts.ac.uk

[3]Department of Physics and Astronomy, Johns Hopkins University, Baltimore, MD 21218, USA; jfulb@skysrv.pha.jhu.edu

[4]Visiting astronomer, Cerro Tololo Inter–American Observatory, National Optical Astronomy Observatory, which are operated by the Association of Universities for Research in Astronomy, under contract with the National Science Foundation.

[5]National Science Foundation Astronomy and Astrophysics Postdoctoral Fellow

initial composition than the inner bulge composition. The [Na/Fe] and to a lesser extent [La/Fe] abundances further indicate that the metal–poor bulge, at least at ∼1 kpc from the Galactic center, and thick disk may not share an identical chemistry.

Subject headings: stars: abundances, Galactic bulge: general, bulge: Galaxy: bulge, stars: Population II

1. INTRODUCTION

It has long been known that stars in the Galactic bulge exhibit an interesting chemical composition. Bulge stars tend to be relatively metal–rich ([Fe/H][1]$\gtrsim$–0.6) like the thin and thick disk, but exhibit larger [α/Fe] ratios than similar metallicity thin disk stars (e.g., McWilliam & Rich 1994; Fulbright et al. 2007; Lecureur et al. 2007; Melendez et al. 2008; Alves–Brito et al. 2010). The first paper in this series (Johnson et al. 2011) confirmed that the [α/Fe] enhancements extend out to at least the Plaut field (b=–8°) we consider here, and that this field follows the declining metallicity gradient with increasing Galactic latitude found by Zoccali et al. (2008). Gonzalez et al. (2011) also find that the uniform [α/Fe] enhancements extend from at least b=–4° to b=–12° along the minor–axis. The pervasive trend of α–enhancement in the bulge is classically considered to reflect early, rapid enrichment due to massive star supernovae (SNe).

Dynamically, the Plaut field stars considered here exhibit cylindrical rotation that is well–modeled by the N–body bar model of Shen et al. (2010). This work suggests that the bulge has its origin in a primordial massive disk, and thus to some extent the bar and inner thick disk may share a largely similar formation history. Recent thick disk and bulge abundance analyses (e.g., Melendez et al. 2008; Alves–Brito et al. 2010; Bensby et al. 2010a; 2011) support this scenario and indicate that the thick disk and bulge may in fact share very similar chemical compositions. However, we note that the bulge may actually be composed of two separate populations, with one similar in metallicity and composition to the thick disk and the other considerably more metal–rich (Babusiaux et al. 2010; Bensby et al. 2010a; 2011; Hill et al. 2011). Additionally, in Johnson et al. (2011) we found that a population of red clump stars, likely belonging to an inner disk population, are as α–enhanced as the bulge red giant branch (RGB) stars but have metallicities and radial velocities consistent with the

[1]We use of the standard spectroscopic notation where [A/B]≡log(N_A/N_B)$_{star}$–log(N_A/N_B)$_\odot$ and log ϵ(A)≡log(N_A/N_H)+12.0 for elements A and B.

thin disk. All of these findings raise the question of whether a unique chemical "tag" for bulge stars exists.

Although the α–element abundance trends seem to indicate that the thick disk and bulge share very similar chemical enrichment histories, the lighter odd–Z and heavier neutron–capture elements offer the possibility of refining our inferences concerning the bulge's chemical evolution timescale relative to other populations. Unlike the α–elements, which are almost solely produced in massive stars, light odd–Z elements like Na and Al can be produced over longer timescales in both massive and intermediate mass stars. Furthermore, their unique abundance signatures in other stellar populations, such as globular clusters, may make it possible to derive constraints on the bulge's merger history. In a similar fashion, the elements heavier than the Fe–peak are mostly produced in either the rapid (r–process) or slow (s–process) neutron–capture processes. While the r–process is thought to be active in core–collapse SNe and thus traces rapid chemical enrichment, the s–process is mostly active in low and intermediate mass thermally pulsing asymptotic giant branch (AGB) stars living $\sim$500 Myr to several Gyr (e.g., see recent review by Sneden et al. 2008 and references therein). Since the production of light odd–Z, α, and heavy elements traces a wide range of timescales, the bulge and thick disk should exhibit comparable abundance trends for all elements if they truly experienced similar formation timescales and enrichment histories.

Therefore, we have measured Na, Al, Zr, La, Nd, and Eu abundances for 39 RGB stars in a single field located near Plaut's low extinction window. We have also analyzed these elements in a similar sample of 23 inner disk red clump stars identified in Johnson et al. (2011). We compare the abundance trends measured here to those available in other bulge fields located at different Galactic latitudes. These comparisons will provide insight into whether the inner and outer bulge experienced any significant formation timescale and/or composition differences. We then compare our results to those available in the literature for the Galactic halo, thick disk, and thin disk. This analysis will help us understand whether the thick disk and bulge are truly chemically indistinguishable, and also yield insight into how the various populations may have influenced the bulge's chemical enrichment.

2. OBSERVATIONS AND DATA ANALYSES

Details of the target selection, observations, data reductions, and previous abundance determinations are provided in Johnson et al. (2011). However, here we provide a brief summary of the critical observation and analysis information necessary for interpreting the results presented in this paper.

We have previously obtained high resolution (R≈25,000), high signal–to–noise (S/N∼50–100 pixel^{-1}) spectra of a combined 92 stars in two separate fields located near Plaut's low–extinction window. All data were obtained using the Blanco 4m telescope instrumented with the Hydra multifiber spectrograph at Cerro Tololo Inter–American Observatory. In Johnson et al. (2011) we derived [Fe/H], [Si/Fe], and [Ca/Fe] ratios via equivalent width (EW) and spectrum synthesis analyses for 61 giants in "Field 1" (l=–1°, b=–8.5°) and [Fe/H] ratios for an additional 31 giants in "Field 2" (l=0°, b=–8°). While we concluded that 38 of the targets observed in Field 1 and all of the targets observed in Field 2 are likely RGB stars belonging to the bulge population, we determined that 23 of the stars in Field 1 are likely foreground red clump stars belonging to an inner disk population. Note however that the population assignments for these 23 stars are not robust, and are based solely on tentative identifications from literature sources (e.g., Zoccali et al. 2003; Vieira et al. 2007; Rangwala et al. 2009).

Although we observed Field 1 in four separate wavelength regions (6000–6250, 6150–6400, 6500–6800, and 7650–7950 Å), Field 2 was only observed in two wavelength regions (6150–6400 and 6500–6800 Å). Given this, and the fact that the S/N ratios for the Field 1 spectra were significantly higher than for Field 2, we only report the additional abundances for Field 1 in this paper. However, there is one star in Field 2 that has been identified as a Li–rich giant (2MASS 18183679–3251454) and we have determined abundances of additional elements, including lithium, for this star.

The model atmosphere parameters for the stars presented here are the same as those listed in Johnson et al. (2011; their Table 1). The effective temperatures ($T_{\rm eff}$) for all stars were derived from dereddened V–K_s colors, and the surface gravities (log g) for the RGB stars were calculated based on each star's bolometric magnitude, assuming a distance of 8 kpc. Since the distances to the foreground red clump stars are not known, their surface gravity values were estimated from the Padova stellar evolutionary tracks (Girardi et al. 2000). Model atmosphere metallicities were set at the derived [Fe/H] ratio for each star, and microturbulence (V_t) was determined by removing trends in Fe I abundance as a function of line strength. The final model atmosphere parameters were then used to interpolate within the α–rich ODFNEW ATLAS9 grid (Castelli et al. 1997[2]).

[2]The model atmosphere grid can be downloaded from http://wwwuser.oat.ts.astro.it/castelli/grids.html.

2.1. Spectrum Synthesis Abundance Determinations

The abundances of all elements analyzed here were determined via spectrum synthesis using a newly modified parallel version of the 2010 LTE line analysis code MOOG[3] (Sneden 1973). The modified code, developed for this project, provides the same interface and abundance algorithms as the original MOOG *synth* driver, but the calculations for different chemical compositions are evenly distributed among individual processing cores via the open message passing interface (Open MPI[4]) communication protocol. The effective result of this parallelization scheme is an overall calculation speed increase to the end user that scales nearly linearly with the number of processing cores being utilized. As in Johnson et al. (2011), all abundance ratios reported here have been calculated relative to Arcturus. A summary of the lines used here and the adopted Arcturus [X/Fe] ratios is provided in Table 1.

2.1.1. Sodium and Aluminum

The abundances of sodium and aluminum were determined using the 6154/6160 Å Na I lines and the 6696/6698 Å Al I lines. The synthesized regions for both line sets spanned 6150–6170 Å for Na and 6690–6705 Å for Al. The log gf values for all significant atomic and molecular lines in these regions were first set in Arcturus by forcing the synthetic spectra to match the high resolution, high S/N Arcturus atlas[5]. All Arcturus abundances were set by adopting the [X/Fe] ratios in Fulbright et al. (2007; their Table 2). Elements not analyzed in Fulbright et al. (2007) were set at the values given in Peterson et al. (1993; their Table 3), and elements not listed in Peterson et al. (1993) were set at [X/Fe]=0. Therefore, the [Na/Fe] and [Al/Fe] ratios listed in Table 2 are measured relative to the Arcturus abundances of [Na/Fe]=+0.09 and [Al/Fe]=+0.38, and the [Fe/H] values for each star are the same as those listed in Johnson et al. (2011; their Table 1).

Given the large metallicity, and to a lesser extent T_{eff} and log(g), range in our sample, it is likely that the Na and Al line profiles in our spectra reflect moderate departures from LTE. However, the subordinate lines used here typically have NLTE corrections $\lesssim$0.10–0.15 dex (e.g., Gratton et al. 1999; Mashonkina et al. 2000; Gehren et al. 2004; Andrievsky et al. 2008; Lind et al. 2011). Unfortunately, there are no "standard" NLTE corrections employed

[3]MOOG can be downloaded at http://www.as.utexas.edu/~chris/moog.html.

[4]Open MPI is freely available and can be downloaded at http://www.open-mpi.org/.

[5]The Arcturus atlas can be downloaded at: http://www.noao.edu/archives.html.

in the literature, in part because the various calculations often utilize different input physics and model atmospheres. Therefore, the [Na/Fe] and [Al/Fe] abundances provided in Table 2 do not include any NLTE corrections, but we caution the reader that any metallicity and/or temperature dependent abundance trends seen in our data, especially those at the level $\lesssim$0.10 dex, could be affected by strictly assuming LTE[6]. Although we have attempted to cancel out many of the model atmosphere dependencies by anchoring our abundance scale to Arcturus, truly self–consistent 3D and NLTE calculations will be needed in order to validate any subtle abundance trends.

2.1.2. Zirconium and Neodymium

The zirconium and neodymium abundances listed in Table 2 are based on an average of the 6134, 6140, and 6143 Å Zr I lines and the 6740 Å Nd II line. Although both of these elements have multiple, stable isotopes of both even and odd mass numbers, we are not aware of any existing hyperfine and/or isotope dependent linelists available in the literature for the transitions used here. However, as discussed below, we have concluded that neglecting these issues should not lead to any significant errors in the derived abundances for either element.

For the case of the Zr I lines, the solar system isotopic ratios presented in Anders & Grevesse (1989; their Table 3) indicate that 51.45% of the total Zr abundance should reside as the even isotope ^{90}Zr, which will not be subject to hyperfine broadening, and the remaining even isotopes (^{92}Zr, ^{94}Zr, and ^{96}Zr) make up a combined 37.33% of the total Zr abundance. The lone stable odd isotope (^{91}Zr) makes up only 11.22% of the total Zr abundance and likely does not contribute a strong broadening effect. We therefore conclude that because the ^{90}Zr, ^{92}Zr, ^{94}Zr, and ^{96}Zr isotopes dominate the line profile no additional corrections are required.

A similar argument can be made for the Nd II measurements. Like zirconium, neodymium is made up of multiple long–lived isotopes, and in the solar system the total neodymium abundance is distributed into ^{142}Nd, ^{143}Nd, ^{144}Nd, ^{145}Nd, ^{146}Nd, ^{148}Nd, and ^{150}Nd in the proportions 27.13%, 12.18%, 23.80%, 8.30%, 17.19%, 5.76%, and 5.64%, respectively (Anders & Grevesse 1989). However, Aoki et al. (2001) and Den Hartog et al. (2003) point out that the odd isotopes constitute little more than 20% of the total Nd abundance and therefore their hyperfine broadening effects are negligible. Similarly, the isotopic broadening for the blue transitions listed in Aoki et al. (2001; their Table A3) do not exceed ∼0.004 Å. Therefore, we assume that the isotope broadening in the 6740 Å Nd II line used here is of

[6]For similar reasons we did not apply NLTE corrections to any other elements analyzed here except Li.

the same order of magnitude and can therefore also be ignored.

Since neither of our adopted "standard" Arcturus abundance scales (Peterson et al. 1993 and Fulbright et al. 2007) report [Zr/Fe] or [Nd/Fe] ratios, we employed a slightly different method for determining the log gf values of the transitions used for these elements. In both cases we started with the log gf values provided by the VALD[7] compilation (Kupka et al. 2000) and set the oscillator strengths based on an inverse solar analysis (i.e., the oscillator strengths were adjusted until the synthetic line profiles matched the observed line profiles in the high resolution, high S/N solar spectrum provided with the Arcturus atlas). The adopted solar abundances are $\log \epsilon$(Zr)=+2.60 and $\log \epsilon$(Nd)=+1.45 (Anders & Grevesse 1989), which are nearly identical to the recommended values provided in Asplund et al. (2009; their Table 1). Finally, we used these log gf values to determine the Zr and Nd abundances for each line in the Arcturus atlas in order to perform a line–by–line differential abundance analysis for the program stars. The average abundance ratios derived for Arcturus were [Zr/Fe]=+0.00 and [Nd/Fe]=+0.05.

2.1.3. Lanthanum and Europium

Unlike the elements listed in §2.1.1–2.1.2, the lines used to derive the [La/Fe] (6262 Å) and [Eu/Fe] (6645 Å) ratios can be affected significantly by hyperfine structure and/or isotopic broadening. The total lanthanum abundance is almost entirely made up of a single stable isotope (^{139}La) so isotopic broadening is not an issue. However, the absorption lines arising from this odd mass number isotope are often strongly affected by hyperfine structure broadening. In order to properly account for this effect in the 6262 Å La II line, we used the laboratory derived hyperfine linelist provided by Lawler et al. (2001a). The reference Arcturus [La/Fe] abundance was set by taking the laboratory log gf values and fitting the 6262 Å La II line profile in the Arcturus atlas. This yielded an Arcturus abundance of [La/Fe]=–0.06, assuming the solar $\log \epsilon$(La)=+1.13, as determined in Lawler et al. (2001a).

Europium is one of the more complex elements to analyze because many of its transitions are significantly affected both by isotopic and hyperfine structure broadening. Although the 6645 Å Eu II line used here is usually relatively weak ($\lesssim$50 mA), it is still important to account for these two effects because failing to do so can lead to systematic errors exceeding 0.1 dex. In order to properly fit the 6645 Å Eu II line we used the linelist provided by Lawler et al. (2001b) and assumed a solar isotopic mix (^{151}Eu=47.8%, ^{153}Eu=52.2%). Similar to the case of La mentioned above, we determined the reference Arcturus [Eu/Fe] abundance

[7]The Vienna Atomic Line Database can be accessed at http://vald.astro.univie.ac.at/∼vald/php/vald.php.

by taking the laboratory log gf values and fitting a synthetic line profile to the 6645 Å Eu II line in the Arcturus atlas. This provided an abundance of [Eu/Fe]=+0.29, assuming the solar log ϵ(Eu)=+0.52 (Lawler et al. 2001b). The final [La/Fe] and [Eu/Fe] ratios for each star are listed in Table 2.

2.1.4. The Li–Rich Giant 2MASS 18183679–3251454

Although the 6707 Å Li I resonance line is typically too weak to be measured in the spectra of evolved RGB stars, one star in our sample (2MASS 18183679–3251454) exhibited a very strong Li line. In order to highlight the unusually strong Li line in this star, which has an EW of 504.3 mÅ, Figure 1 illustrates the stark difference in Li line strengths between 2MASS 18183679–3251454 and another star in our sample with similar T_{eff}, log(g), and [Fe/H]. Unlike the elements mentioned above, we did not measure the Li abundance relative to Arcturus because the 6707 Å line strengths between 2MASS 18183679–3251454 and Arcturus are significantly different. Instead, we adopted the linelist of Hobbs et al. (1999). While lines of both ^{6}Li and ^{7}Li are blended in the spectra of dwarf stars, the Li present in this star is not primordial and is likely dominated by ^{7}Li. We therefore derived a Li abundance from spectrum synthesis assuming that ^{7}Li is the dominant isotope. The final derived LTE abundance is log ϵ(Li)=+3.56. Fortunately, the NLTE correction is small (Lind et al. 2009), and the NLTE Li abundance decreases only slightly to log ϵ(Li)=+3.51.

Given the lower S/N and limited spectral coverage for this star, it is difficult to determine whether 2MASS 18183679–3251454 exhibits any other unusual spectral features. However, examination of Table 2 (and the subsequent figures) suggests it may have slightly lower [Al/Fe] and [Eu/Fe] ratios than the other Plaut field stars but normal [La/Fe]. Interestingly, the combined datasets of McWilliam & Rich (1994), Gonzalez et al. (2009), Lebzelter et al. (2012), and the present study have found seven Li–rich giants out of a sample of ∼850 bulge stars. This suggests that the fraction of Li–rich giants in the bulge is ∼1%, and is comparable to what is found in other stellar populations (e.g., Brown et al. 1989; Kraft et al. 1999; de La Reza et al. 1997; Ruchti et al. 2011).

2.2. Abundance Error Estimates

In Table 3 we list the estimated log ϵ(X) abundance uncertainties for each element (except Li) measured in all stars. We provide individual abundance sensitivities to model atmosphere parameter uncertainties of ΔT_{eff}+100 K, Δlog(g)+0.3 dex, Δ[M/H]+0.3 dex,

ΔV_t+0.3 km s^{-1}, and also include the measured line–to–line dispersion for each element in each star. Note that for elements and/or stars where only a single line was available to measure we have assigned a default line–to–line dispersion of 0.07 dex. This value is equal to the average line–to–line dispersion of all instances where more than one line was measured. A final estimate of the total uncertainty for each element is also included in Table 3.

Although the average total abundance uncertainties tend to range from ∼0.15–0.20 dex, it is likely that these represent conservative upper limits. In Johnson et al. (2011) we concluded that values of ΔT_{eff}+50 K and Δ[M/H]+0.16 dex might be more appropriate. The T_{eff} uncertainty was estimated by assuming that the E(B–V) values were accurate to within ±15%, which equaled the E(B–V) dispersion across the full Hydra field–of–view. We also note that the dispersion in the Alonso et al. (1999) V–K_s color–temperature relation used here is only 25 K. The [M/H] uncertainty of 0.16 dex was based on the average log ϵ(Fe) line–to–line dispersion. However, it seems likely that a microturbulence uncertainty of 0.3 km s^{-1}, especially for more metal–rich stars with stronger lines, is a reasonable assumption. For bulge field stars, the surface gravity is often the most difficult model parameter to constrain. While we assumed a fixed distance of 8 kpc, it is likely that an individual bulge star's distance may range anywhere from ∼6–10 kpc (e.g., see Zoccali et al. 2008, their Figure 10). This corresponds to a change in derived log(g) of ∼0.2–0.25 dex, which makes the Δlog(g) of 0.3 dex used here an appropriate (though possibly conservative) choice. On the other hand, distances to the foreground red clump stars are almost completely unconstrained. However, assuming the stars actually belong to the red clump means they should have surface gravities close to log(g)∼2.3, and therefore their true surface gravities probably do not exceed the 0.3 dex range estimated in Table 3.

Examination of Table 3 reveals that not all elements are equally affected by model atmosphere parameter uncertainties. While changes in T_{eff} noticeably affect the abundances derived from neutral species (Na, Al, and especially Zr), the abundances derived from singly ionized species (La, Nd, and Eu) are affected at $\lesssim$0.03 dex level. In contrast, changes to the model atmosphere surface gravity and metallicity can strongly affect the singly ionized species but have a nearly negligible influence on the abundances derived from neutral species. Note that the [La/Fe], [Nd/Fe], and [Eu/Fe] ratios provided in Table 2 are measured relative to Fe I rather than Fe II. While this is not necessarily a problem as long as the surface gravities are accurate, the increased sensitivity to surface gravity means that one should use caution when interpreting small abundance differences related to the La, Nd, and Eu trends. Microturbulence uncertainties have a very small affect on most lines in metal–poor stars because the lines are weak and on the linear portion of the curve–of–growth. However, Table 3 illustrates the growing role microturbulence plays with increasing metallicity and line strength. In the most metal–rich stars, abundances of Na, Al, and Zr can be affected

at the >0.1 dex level while the influence on singly ionized species is typically <0.05 dex in magnitude.

3. RESULTS

3.1. The Light Elements: Sodium and Aluminum

In addition to the often used [α/Fe] ratio, the two light odd–Z elements Na and Al can be exploited as sensitive tracers of a stellar population's chemical enrichment history. Na and Al production can have multiple sources tracing timescales ranging from $\lesssim$30 Myr to more than several Gyr. While most of the Na and Al in the Galaxy is produced during the hydrostatic helium, carbon, and neon burning stages of massive stars (e.g., Arnett & Thielemann 1985; Thielemann & Arnett 1985; Woosley & Weaver 1995), these elements can also be created via the NeNa and MgAl proton–capture cycles active in the envelopes of massive and intermediate mass stars (e.g., Decressin et al. 2007; Ventura & D'Antona 2009; Karakas 2010) and near the hydrogen–burning shells of some lower mass RGB stars (e.g., Sweigart & Mengel 1979; Denisenkov & Denisenkova 1990; D'Antona & Ventura 2007). However, the photospheric [Na/Fe] and [Al/Fe] ratios measured in bulge RGB stars are likely not significantly altered by *in situ* processing because their relatively high metallicity ([Fe/H]$\gtrsim$–0.6, on average) does not provide favorable conditions for efficient NeNa and/or MgAl cycling and deep *in situ* mixing (e.g., D'Antona & Ventura 2007). Therefore, it is probably a safe assumption that our derived photospheric [Na/Fe] and [Al/Fe] ratios reflect the stars' original composition, which resulted purely from external pollution.

In Figure 2 we plot the abundance trends of [Na/Fe], [Al/Fe], and (for reference) the [α/Fe] abundances from Johnson et al. (2011) as a function of [Fe/H]. At the low metallicity end ([Fe/H]$\lesssim$–0.8), Na and Al are generally under– and over–abundant at [Na/Fe]$\sim$–0.3 and [Al/Fe]$\sim$+0.2, respectively. If the three anomalously low Na and Al stars (2MASS 18182256–3401248, 2MASS 18174351–3401412, and 2MASS 18183521–3344124) are excluded, then the [Na/Fe] and [Al/Fe] abundance trends are essentially flat between –1.5$\lesssim$[Fe/H]$\lesssim$–0.8. However, the origin of these three low Na and Al stars is unclear, but each could have been captured from the Galactic halo or a disrupted stellar system, such as a globular cluster or dwarf galaxy (see also §4.2.1). Although these three stars span a relatively narrow metallicity range ([Fe/H]=–1.02 to –0.79), they exhibit a large radial velocity range from –25 to +49 km s^{-1}. This suggests that the stars probably did not all originate from a single globular cluster, assuming the initial kinematics are preserved. Interestingly, the other peculiar metal–poor stars in Figure 2 (blue outlined pentagons), which have large neutron–capture element enhancements, mostly follow the same [Na/Fe], [Al/Fe], and [α/Fe] trends as the other bulge

giants.

While the general [Na/Fe] and [Al/Fe] trends are relatively flat at [Fe/H]$\lesssim$–0.8, the behavior of [Na/Fe] and [Al/Fe] begins to differentiate at higher metallicities. This is naturally expected from the metallicity dependence of yields for odd–Z elements, which depend on the surplus of neutrons from ^{22}Ne and therefore on the initial CNO abundance. As can be seen in Figure 2, Al tends to mimic the α–element trend such that the average [Al/Fe] ratio remains both moderately enhanced and constant until [Fe/H]$\sim$–0.2, where it then begins to decline. The only exception appears to be the lone Li–rich giant (filled green box), which exhibits a moderately low [Al/Fe]=–0.05. On the other hand, the average Na abundance increases from [Na/Fe]$\sim$–0.3 to +0.3 over that same range in [Fe/H], and then remains roughly constant at [Fe/H]$\gtrsim$–0.2.

Although the targets identified as possible inner disk red clump stars (filled cyan circles) show a nearly identical [α/Fe] trend as the bulge RGB stars, it is difficult to determine whether their [Na/Fe] and [Al/Fe] distributions are unique. Visual inspection of Figure 2 indicates that there may be a tendency for the clump stars to have systematically lower [Na/Fe] but similar [Al/Fe] ratios compared to bulge RGB stars of the same metallicity. A quantitative comparison between the two samples shows that the bulge RGB stars with [Fe/H]>–0.4 have $\langle$[Na/Fe]$\rangle$=+0.19 (σ=0.20) and $\langle$[Al/Fe]$\rangle$=+0.15 (σ=0.17) while the clump stars have $\langle$[Na/Fe]$\rangle$=+0.05 (σ=0.25) and $\langle$[Al/Fe]$\rangle$=+0.07 (σ=0.11). However, two–sided Kolmogorov–Smirnov tests (Press et al. 1992) comparing the [X/Fe] distributions of the RGB and clump stars are unable to confidently reject the null hypothesis that the [Na/Fe] and [Al/Fe] samples are drawn from the same parent population.[8]

In Figure 3 we show [Na/Fe] versus [Al/Fe] and the [Na/Al] ratio as a function of [Fe/H]. A well–known correlation exists between [Na/Fe] and [Al/Fe] in Galactic globular clusters (e.g., see review by Gratton et al. 2004), and it is believed that this correlation is driven primarily by the mixing of pristine gas with material that has been enriched with the by–products of the NeNa and MgAl proton–capture cycles. However, as can be seen in Figure 3, the RGB and clump stars analyzed here do not show significant evidence for the existence of a Na–Al correlation. This is supported by the relatively weak Pearson (R_p) and Spearman (R_s) correlation coefficients for the data (R_p=0.298 and R_s=0.252), excluding obvious outliers in the distribution. Although there does not appear to be a strong correlation between [Na/Fe] and [Al/Fe], the [Na/Al] ratio plotted as a function of [Fe/H] shows a relatively steep trend such that [Na/Al] increases with metallicity. Both the bulge giants and the foreground

[8]We adopt the notion that the null hypothesis (i.e., that the two distributions are the same) can be rejected if the p value is "small" (<0.05). For both [Na/Fe] and [Al/Fe] distributions the p values are >0.20.

clump stars appear to share this chemical trait. Note that the three metal–poor stars with low [Na/Fe] and [Al/Fe] ratios no longer appear as outliers in the distribution when Na is normalized to Al. This suggests that at least the Na and Al in these stars may share a common production origin with the rest of the metal–poor bulge giants.

3.2. The Neutron–Capture Elements: Zirconium–Europium

Unlike the lighter elements, which are produced predominantly through charged–particle reactions, most of the isotopes of elements heavier than the Fe–peak are produced through successive neutron captures on preexisting seed nuclei (e.g., see the recent review by Sneden et al. 2008). Heavy element production typically occurs through one of two pathways: the slow neutron–capture process (s–process), which is active at low neutron exposure rates, and the rapid neutron–capture process (r–process), which is active at high neutron exposure rates. In general, each process is responsible for synthesizing about half of the stable heavy element isotopes, but many isotopes can also be produced through both processes (e.g., Burris et al. 2000; their Table 5). Furthermore, each general production mechanism can be deconvolved into subprocesses that predominantly produce a set mass range of nuclei.

The s–process is typically divided into three subcomponents: the "main", "weak", and "strong" s–processes. The products of the main component, nuclei in the range $88 \lesssim A \lesssim 208$ (e.g., Käppeler 1989; Arlandini et al. 1999), are the most commonly studied in the literature. This s–process mechanism is believed to be active in $\sim$1.5–4.0 $M_{\odot}$ thermally pulsing AGB stars (e.g., Busso et al. 1999; Herwig 2005; Straniero et al. 2006), and may be responsible for some fraction of the elements Zr, La, and Nd analyzed here. While the main component is thought to become active over relatively long timescales ($\gtrsim$500 Myr), the weak s–process may be active as little as $\sim$10 Myr after the onset of star formation. The environmental and nucleosynthesis details for the weak s–process are not as well understood as those of the main s–process, but it is believed to be active in $>$10 $M_{\odot}$ stars during the He–burning (e.g., Peters 1968; Lamb et al. 1977; Prantzos et al. 1987; Langer et al. 1989; Prantzos 1990; Raiteri et al. 1991a) and C–burning stages (e.g., Arcoragi et al. 1991; Raiteri et al. 1991b; Raiteri et al. 1993; The et al. 2007; Pignatari et al. 2010).[9] This production mechanism is typically used to explain the enhanced abundances of isotopes in the mass range $60 \lesssim A \lesssim 90$, found in some metal–poor stars (e.g., Burris et al. 2000). The Zr analyzed here may have some production via the weak s–process. Lastly, the strong s–process component is invoked

[9]Note that low metallicity, rapidly rotating stars may also be able to selectively produce the "light" s–process elements Y, Sr, and (possibly) Zr, due to enhanced rotational mixing (Chiappini et al. 2011).

to explain approximately half of the production of ^{208}Pb, and is also thought to be active in low and intermediate mass, low metallicity AGB stars (e.g., Clayton & Rassbach 1967; Beer & Macklin 1985; Gallino et al. 1998). However, it is unlikely that any of the elements analyzed here have been significantly affected by the strong s–process.

In a similar fashion to the s–process, the r–process can be differentiated into two different mechanisms: the "main" and "weak" processes. While the exact sources of these two r–process components are not currently known, both are strongly suspected to be associated with the final stages of massive stars exploding as core–collapse SNe (e.g., Lattimer et al. 1977; Truran 1981; Mathews & Cowan 1990; Cowan et al. 1991; Takahashi et al. 1994; Woosley et al. 1994; Freiburghaus et al. 1999; Truran et al. 2002; Arnould et al. 2007). Although the main r–process is responsible for the production of many isotopes with A$\gtrsim$130–140, the weak r–process component is believed to only produce isotopes with A$\lesssim$130–140. In particular, the weak r–process mechanism is typically invoked in order to explain the existence of certain metal–poor stars exhibiting preferential enhancement of only the r–process nuclei near the Sr–Y–Zr peak (e.g., McWilliam 1998; Burris et al. 2000; Johnson & Bolte 2002; Travaglio et al. 2004; François et al. 2007; Honda et al. 2007). For the present work the main r–process may affect the abundances of La, Nd, and especially Eu, and the weak r–process may contribute to the production of Zr.

3.2.1. Zirconium

In Figure 4 we show a plot of [Zr/Fe] as a function of [Fe/H] for all stars analyzed here. If we ignore the three super Zr–rich stars, then the remaining stars in our sample with [Fe/H]<–0.9 have a nearly uniform Zr abundance of $\langle$[Zr/Fe]$\rangle$=+0.01 (σ=0.04). In the range [Fe/H]=–0.8 to –0.4 there is some evidence of two separate sequences, where one group of stars is enhanced at [Zr/Fe]$\sim$+0.25 and the other is moderately Zr–poor at [Zr/Fe]$\sim$–0.10. Interestingly, these two distributions merge together at [Fe/H]$\approx$–0.4 and continue a trend of decreasing [Zr/Fe] abundance with increasing [Fe/H] down to [Zr/Fe]$\sim$–0.3 at [Fe/H]$\sim$+0.3. However, the larger errors associated with the Zr I measurements makes it difficult to assess how robust the difference is between the "Zr–enhanced" and "Zr–poor" stars. The clump stars do not appear to exhibit any strong trends in [Zr/Fe] as a function of [Fe/H] and instead have an average abundance of $\langle$[Zr/Fe]$\rangle$=–0.08 but with a relatively large star–to–star scatter (σ=0.19). A two–sided KS test cannot rule out that the RGB and clump [Zr/Fe] distributions are significantly different at [Fe/H]>–0.4.

3.2.2. Lanthanum, Neodymium, and Europium

In Figure 5 we plot the [La/Fe], [Nd/Fe], and [Eu/Fe] ratios for all stars as a function of [Fe/H]. First examining La and Nd, it is clear from Figure 5 that both elements exhibit very similar abundance trends (with a ∼0.1–0.2 dex systematic offset). On the metal–poor end, nearly all stars are enhanced at [La,Nd/Fe]≈+0.30. At metallicities greater than [Fe/H]=–0.80, the [La/Fe] and [Nd/Fe] trends decline with increasing metallicity until [Fe/H]∼–0.4. Beyond [Fe/H]=–0.4, the [La,Nd/Fe] ratios remain roughly constant at [La,Nd/Fe]∼–0.30. Although the star–to–star scatter is larger for the clump stars, there is some indication that the clump stars may have higher [La/Fe] and [Nd/Fe] abundances than the bulge giants. In the metallicity regime covered by the clump stars ([Fe/H]$\gtrsim$–0.4), the bulge stars have $\langle$[La/Fe]$\rangle$=–0.29 (σ=0.14) and $\langle$[Nd/Fe]$\rangle$=–0.14 (σ=0.17) while the clump stars have $\langle$[La/Fe]$\rangle$=–0.10 (σ=0.19) and $\langle$[Nd/Fe]$\rangle$=–0.03 (σ=0.20). Interestingly, a two–sided KS test suggests that the clump and RGB [La/Fe] distributions might be drawn from different parent populations, but the case for [Nd/Fe] is not as strong with a p–value of 0.09 (compared to 0.01 for La). If larger sample sizes confirm this result then it may be possible that the [La/Fe] and [Nd/Fe] ratios could be used as sensitive discriminators between the bulge and inner disk populations, assuming the clump stars identified here are actually part of the inner disk.

For Eu, inspection of Figure 5 reveals that [Eu/Fe] exhibits a different trend than La and Nd. Although Eu is also enhanced in the metal–poor stars at [Eu/Fe]∼+0.30, the overall shape of the [Eu/Fe] versus [Fe/H] trend follows a much more "α–like" distribution. Like the [α/Fe] distribution shown in Figure 2, [Eu/Fe] remains enhanced at [Eu/Fe]∼+0.30 until [Fe/H]∼–0.4 where [Eu/Fe] then begins to decline at higher metallicities. In fact, overplotting [Eu/Fe] and [α/Fe], as is shown in Figure 6, illustrates the remarkable agreement between the distributions of these two elements. The similar behavior between the α elements and Eu is not unexpected since both groups are believed to be produced by massive stars. It is also worth noting that while the clump stars may potentially have different [La/Fe] and [Nd/Fe] abundances than the bulge RGB stars, there does not appear to be any significant difference between the two populations with respect to the [Eu/Fe] (or [α/Fe]) distributions.

The [La/Eu] ratio is often used as a tracer of the relative contributions the r– and s–processes have made to a stellar population. This indicator is useful because La can be made in both processes, but Eu is made almost entirely by the r–process (∼97%; e.g., Burris et al. 2000). Similarly, when the s–process is active plots of the "heavy" (e.g., Ba and La) versus "light" (e.g., Y and Zr) s–process elements can yield insight into the metallicity of the production site. The s–process in a metal–poor environment is expected to produce a higher heavy/light ratio because there are more neutrons available per seed nucleon and

the neutron–capture chain proceeds to heavier nuclei. In Figure 7 we plot the [La/Eu] and [La/Zr] ratios as a function of [Fe/H] for all program stars. We find that the [La/Eu] trend, especially for [Fe/H]>–0.8, is nearly flat at $\langle$[La/Eu]$\rangle\sim$–0.3 and exhibits a relatively consistent star–to–star scatter (σ=0.15). The consistency of the [La/Eu] magnitude and scatter across a wide range in [Fe/H] suggests that the abundance variations are likely dominated by measurement errors. The low [La/Eu] ratios are consistent with the r–process being the dominant neutron–capture production process for nearly all of the bulge RGB stars[10]. However, several of the most metal–poor stars appear to have [La/Eu] ratios that are higher than the bulk of the RGB population. This suggests that at least some of the most metal–poor bulge stars may have experienced enrichment by the s–process, and is supported by the enhanced [La/Zr] ratios in these same stars. In a similar fashion, the relatively flat [La/Zr] trend of the more metal–rich RGB stars may be consistent with the absence of a significant s–process contribution. However, we note again that the larger errors on the Zr abundance may be masking any subtle, underlying trends. Interestingly, while the clump stars do not seem to significantly differentiate themselves from the bulge RGB population in the [La/Zr] plot, these stars appear to exhibit a non–negligible rise in the [La/Eu] ratio at [Fe/H]>0. If confirmed, then this may be evidence for a longer formation timescale in the inner disk compared to the Galactic bulge.

4. DISCUSSION

4.1. Comparison to Other Bulge Field Locations

4.1.1. The Light Elements

In Figure 8 we compare the [Na/Fe], [Al/Fe], and [Na/Al] ratios as a function of [Fe/H] for our data and those available in the literature. First examining [Na/Fe], all regions of the bulge represented in Figure 8 (essentially the minor–axis from b=–4° to b=–12°) generally follow the same abundance pattern. In particular, the average [Na/Fe] ratio increases as a function of metallicity with little change in the star–to–star dispersion. On average, the [Na/Fe] abundance appears to rise from [Na/Fe]$\sim$–0.20 to +0.00 at low metallicity and increase up to [Na/Fe]$\sim$+0.20 to +0.40 at the high metallicity end. Even considering the differences in measurement techniques, data quality, and temperature/gravity regimes covered

[10]Note that star 2MASS 18174742–3348098 exhibits a [La/Eu] ratio that is consistent with pure s–process production. However, given the apparent dominance of the r–process in bulge stars, it seems likely that this star is the result of mass transfer from an AGB companion or was captured from an external stellar system.

by the points in Figure 8, we find no evidence supporting a strong minor–axis abundance gradient in [Na/Fe]. This finding is consistent with the lack of any gradient in [α/Fe].

However, there could be subtle differences at the metal–poor and metal–rich ends of the distribution. Although the number of abundance measurements for stars with [Fe/H]<–1 is small, Figure 8 indicates that the [Na/Fe] ratios for the most metal–poor Plaut field stars (ignoring the three very low Na and Al stars) may be 0.1–0.3 dex lower than those found at b$\lesssim$–4°. If this result is confirmed by larger sample sizes then it could be an indication of composition inhomogeneities in the early bulge. The cause of the discrepancies at the metal–rich end of the [Na/Fe] distribution, noting especially the large range of derived [Na/Fe] ratios, is unclear. Combining all literature data with the present study indicates that stars with [Fe/H]>0 fall into the range –0.3$\lesssim$[Na/Fe]$\lesssim$+1.0, though we note that only Lecureur et al. (2007) find a significant number of stars with [Na/Fe]>+0.5. It may be the case that the larger dispersion seen at [Fe/H]>0 simply reflects the difficulty in accurately analyzing cool, metal–rich giants.

The [Al/Fe] distribution is nearly identical for all bulge stars shown in Figure 8, at least in the range –1.5$\lesssim$[Fe/H]$\lesssim$–0.2. Specifically, the stars tend to be enhanced at [Al/Fe]$\sim$+0.2, regardless of metallicity and bulge location. Although the Lecureur et al. (2007) [Al/Fe] data again show higher abundances and increased star–to–star scatter, the general trend of enhanced [Al/Fe] with no strong metallicity dependence appears to be the same. However, two different [Al/Fe] trends emerge at [Fe/H]$\gtrsim$–0.2. The Plaut field and microlensed dwarfs exhibit a decrease in [Al/Fe] toward solar values, but the data from McWilliam & Rich (1994), Fulbright et al. (2007), Lecureur et al. (2007), and Alves–Brito et al. (2010) consistently show enhanced [Al/Fe] at all metallicities. This is a particularly puzzling problem because the stars contributing to the two separate trends essentially sample the same regions of the bulge.

As is noted in Bensby et al. (2011) and can be seen in Figure 8, two of the metal–rich microlensed bulge dwarfs exhibit higher [Al/Fe] (and [Na/Fe]) abundances than the other dwarfs of similar metallicity. Interestingly, the higher [Al/Fe] ratios of these two stars match the enhancements observed in bulge giants by McWilliam & Rich (1994), Fulbright et al. (2007), Lecureur et al. (2007), and Alves–Brito et al. (2010). These two dwarfs, coupled with the literature data, might hint that two different populations of metal–rich bulge stars exist. Alternatively, the true [Al/Fe] distribution for the metal–rich bulge may span a range from roughly [Al/Fe]=–0.10 to +0.40, and the microlensed dwarf and Plaut data happen to predominantly sample the low–Al stars. There could also be age and/or initial mass function (IMF) variations that contributed to the different abundance trends.

Most analyses tend to find that the bulge is at least 10 Gyr old with a $\sim$1 Gyr age

spread (e.g., Ortolani et al. 1995; Feltzing & Gilmore 2000; Kuijken & Rich 2002; Zoccali et al. 2003; Clarkson et al. 2008), but the data do not fully rule out the existence of a young, metal–rich bulge population (see also Nataf & Gould 2011). In fact, several of the microlensed dwarfs are estimated to be only ∼3–4 Gyr old. While we do not have explicit age estimates for the Plaut field stars, in Johnson et al. (2011) we used old globular cluster isochrones to photometrically estimate the metallicity distribution function in Plaut's field from RGB–tip stars and found excellent agreement with the spectroscopic metallicities. Therefore, we assume that most, if not all, of the RGB stars are old. It is worth noting that the two metal–rich [Al/Fe] enhanced dwarfs seen in Figure 8 have estimated ages of ∼3 and 13 Gyr, and plotting [Al/Fe] versus age for all of the data in Bensby et al. (2010a; 2011) indicates that the two parameters are not strongly correlated. This suggests that age is not a primary cause of the metal–rich [Al/Fe] discrepancy.

In order to investigate whether IMF variations could cause [Al/Fe] differences, we have plotted the data from Figure 8, along with three chemical enrichment models for the Galactic bulge, in Figure 9. The star formation rates are modified from Kobayashi et al. (2006; 2011) to meet the observed metallicity distribution function and include updated super–solar metallicity yields (up to Z=0.05) and nuclear reaction rates. The three models are calculated for a Kroupa (2008) IMF (x=1.3), an extreme top–heavy IMF (x=0.3), and an extreme bottom–heavy IMF (x=1.6). The star formation, infall, and galactic wind timescales are (0.2 Gyr, 5 Gyr, 3 Gyr) for x=1.3, (0.01 Gyr, 5 Gyr, Inf.) for x=0.3, and (0.01 Gyr, 5 Gyr, 1 Gyr) for x=1.6, respectively. As can clearly be seen in Figure 9, the models predict that stars with [Fe/H]>–0.2 originating from populations with different IMFs should exhibit significantly different light element abundances. However, in Figure 10 we plot [α/Fe] as a function of [Fe/H] from several studies spanning the same regions of the bulge as those in Figures 8–9. Figure 10 reiterates the conclusions from Johnson et al. (2011) and Gonzalez et al. (2011) that the [α/Fe] ratio trends are essentially identical for all bulge stars. Since the α–elements are produced almost exclusively in massive stars, these data suggest that there were not any significant IMF variations in the bulge. Additionally, formation timescale differences should also be ruled out from the [α/Fe] trends. In §4.1.2 we show that the heavy element abundances indicate that the enrichment timescale was probably very similar throughout the bulge.

Since the [Na/Fe] and [Al/Fe] ratios alone may be sensitive to parameters such as model atmosphere deficiencies and 3D/NLTE corrections, we have also plotted the [Na/Al] ratio in Figures 8–9 in an attempt to mitigate these effects. Similar to what was observed in Figure 3, we find that normalizing Na by Al generally decreases the star–to–star scatter in a given metallicity bin. While the agreement is very good in the range –0.8$\lesssim$[Fe/H]$\lesssim$–0.2, the slope of the [Na/Al] increase is steepest for the Plaut field data followed by the Lecureur et al.

(2007), Bensby et al. (2010a; 2011), and finally the Baade's window data by McWilliam & Rich (1994), Fulbright et al. (2007), and Alves–Brito et al. (2010). The reason for the [Na/Al] differences is not immediately clear, and the Lecureur et al. (2007) data, which span multiple bulge fields at various Galactic latitudes, do not show any correlations between [Na/Al] ratio and location. Interestingly, the chemical enrichment models shown in Figure 9 have two important predictions: (1) the [Na/Al] ratio should rise with metallicity and (2) this ratio should be nearly independent of the IMF. While the data do clearly exhibit an increase in [Na/Al] with [Fe/H], all of the models predict that the rise should occur at [Fe/H]$\lesssim$–1; however, this is not observed until at least [Fe/H]=–0.4. Additionally, the model [Na/Al] ratios are typically at least 0.2 dex higher than the observed values. However, the yields of these elements are subject to significant changes as the models improve to include newer/updated input physics, nuclear reaction rates, and employ fully self–consistent 3D treatments of parameters such as rotation and convection. Although the [Na/Al] distribution seems to reinforce the previously stated notion that IMF variations are not the cause of the metal–rich abundance differences, other factors such as inflow/outflow of gas could play an important and unaccounted for role. On the other hand, these differences may simply reflect the difficulty in analyzing metal–rich spectra.

4.1.2. The Heavy Elements

In Figure 11 we compare the abundances of [Zr/Fe], [La/Fe], and the "heavy–to–light" ratio ([hs/ls]) versus [Fe/H] between our data and those available in the literature.[11] Since few [Zr/Fe] and [La/Fe] measurements exist for bulge stars in the literature, we have substituted [Y/Fe] and [Ba/Fe] abundances when appropriate. While there is likely to be some systematic offset between [Y/Fe] and [Zr/Fe] or [Ba/Fe] and [La/Fe], these element pairs are neighbors in atomic number and are believed to trace very similar production mechanisms.

We generally find good agreement between all of the data sets plotted in Figure 11. Specifically, it appears that the heavier neutron–capture elements Ba and La exhibit a general trend of decreasing abundance as a function of increasing metallicity, but the Y and Zr trends are much more shallow. The literature and Plaut field data all include a handful of stars with enhanced [Y,Zr/Fe] ratios that deviate from the otherwise relatively flat distribution, but the small sample sizes per metallicity bin, especially on the metal–poor end, make it difficult to understand the origin of these enhanced stars. Many of the stars that appear

[11]A detailed discussion of Nd abundance trends is omitted because very few Nd measurements are available in the literature.

to be enhanced in Y and/or Zr do not stand out as outliers in the Ba and La plot. It is possible that the Y/Zr–enhanced stars could have been stochastically affected by the weak s– and/or r–processes, which are believed to selectively produce elements near the Sr–Y–Zr peak without affecting heavier elements like Ba and La (see the brief discussion in §3.2). The multiple possible production mechanisms for Y and Zr compared to Ba and La, which are only thought to be produced in the main s– and r–processes, may be an explanation for the slightly different abundance trends. Similarly, since Y and Zr may be produced in a wider range of stars than Ba and La, particularly in the weak s–process by massive stars also producing Fe, this may explain why the [Y,Zr/Fe] ratio remains roughly constant over a large metallicity range while the average [Ba,La/Fe] ratio experiences a steady decline at [Fe/H]>–0.8.[12] However, more observations are needed and we note that many of the Zr and Y abundances shown in Figure 11 have uncertainties >0.2 dex.

While more than 70% of the Ba and La in the solar system is thought to have been produced by the main s–process in ∼1.5–4 $M_{\odot}$ thermally pulsing AGB stars (e.g., Burris et al. 2000; Bisterzo et al. 2010), a non–negligible 15–30% is still produced by the r–process. If the bulge formed in $\lesssim$1 Gyr then it is possible that not enough time was available for significant s–process enrichment. Therefore, we may be able to assume that the [Ba,La/Fe] trend shown in Figure 11 mostly reflects metallicity dependent r–process yields. Alternatively, it is possible that only a specific mass range of stars produces Ba and La via the r–process, and the declining trend is a result of Fe but not Ba or La being produced. Interestingly, nearly all of the data points agree that the [Ba,La/Fe] ratios in the most metal–poor bulge stars are enhanced at [Ba,La/Fe]∼+0.2 dex. Could the initially high [Ba,La/Fe] ratios reflect pre–enrichment of the early bulge gas? As we will show in §4.2.2, the most metal–poor bulge stars do in fact fall in the range of observed [La/Fe] abundances for the most metal–rich Galactic halo stars. Furthermore, the slightly enhanced [hs/ls] ratios in the most metal–poor stars suggest that some s–process enrichment occurred. Unfortunately, little is quantitatively known about the pure r–process yields at [Fe/H]>–1.5. However, the main s–process is predicted to produce significant variations in the [hs/ls] ratio as a function of metallicity (e.g., Bisterzo et al. 2010; their Figure 11). Therefore, we can speculate that the general invariance of the [hs/ls] ratio at [Fe/H]$\gtrsim$–1 may be additional evidence that the main s–process did not play a major role in the bulge's chemical enrichment.

Since Eu is believed to be produced almost exclusively in massive stars, the naive expectation is that the trend of [Eu/Fe] versus [Fe/H] should closely mimic that of [α/Fe]. In fact, at least in the Plaut field, we find that the [Eu/Fe] and [α/Fe] trends are nearly

[12]Note that this may not be true if the weak s–process is mostly active in lower mass SNe, which do not produce much Fe.

indistinguishable (see Figure 6). In Figure 12 we plot [Eu/Fe] and [La/Eu] versus [Fe/H] for the Plaut field and the Baade's window data from McWilliam & Rich (1994) and McWilliam et al. (2010), and note that all three data sets exhibit nearly identical [Eu/Fe] trends following the general [α/Fe] distribution. While there is some discrepancy at [Fe/H]>0, we believe this may be related to different studies normalizing Eu II with Fe I (our data) or Fe II (McWilliam & Rich 1994; McWilliam et al. 2010) and/or the small sample size of our data at high metallicity. As was pointed out in McWilliam et al. (2010), the standard Tinsley (1979) chemical enrichment picture implies that the downturn in [α/Fe] and [Eu/Fe] are due to the addition of Fe from Type Ia SNe, and suggests a $\gtrsim$1 Gyr formation timescale for the bulge. However, very little is known about the exact production location of the r–process, and detailed yield calculations do not exist. Therefore, we reach the same conclusion as McWilliam et al. (2010) that the downturn in [Eu/Fe] is likely related more to the metallicity dependent yields of the r–process than the Type II/Type Ia SN ratio.[13]

While the [La/Fe] and [Eu/Fe] ratios may not individually reveal the strength of s– and r–process contributions, the [La/Eu] ratio is predicted to be a strong indicator of the main r–process versus the main s–process contributions. Additionally, normalizing La II by Eu II should cancel out any significant errors associated with measuring La II and Eu II relative to Fe I or Fe II. As can be seen in Figure 12, a majority of bulge stars exhibit [La/Eu] ratios that are consistent with the r–process being the dominant neutron–capture production mechanism. Additionally, the [La/Eu] trends at b=–4° and b=–8° are nearly identical and do not show any indication of an increase in [La/Eu] with rising [Fe/H]. These observations suggest that the enrichment timescales for the inner and outer bulge were very similar and that this enrichment occurred on a timescale rapid enough (probably $\lesssim$1 Gyr) to avoid significant contributions from the main s–process. The nearly indistinguishable [La/Fe] and [Nd/Fe] trends shown in Figure 5 also support the lack of a main s–process contribution. In the solar system, roughly 50% of the Nd is produced by the main s–process (compared to ∼75% for La), and if it were contributing to the bulge's chemical enrichment then we might expect to observe a change in the [Nd/Fe] compared to [La/Fe] trends.

At first glance, it seems as if the [La/Eu] and [α/Fe] data produce conflicting views on the bulge's formation. The [La/Eu] ratios indicate that star formation in the bulge was relatively rapid, but the [α/Fe] data suggest a more extended star formation period that allowed Type Ia SNe to contribute. Unfortunately, the actual timescale over which Type Ia SNe become important is not well constrained and may range from as little as a few

[13]If the bulge stars, even at high metallicity, are in fact dominated by the r–process, then the bulge may prove to be a useful population for examining the r–process at high metallicity. In principle, this is difficult to do with thin and thick disk stars because of contamination by the s–process.

hundred Myr (e.g., Matteucci & Recchi 2001; Raskin et al. 2009) to a few Gyr (e.g., Yoshii et al. 1996). Additionally, there is likely to be a non–negligible metallicity dependence in the yields of α–elements from Type II SNe. In fact, most Type II SN models show a trend of decreasing [α/Fe] yields with increasing metallicity (e.g., Kobayashi et al. 2006; their Figure 5). However, it remains to be seen what role the Type II/Ia SN ratio played in the bulge's chemical enrichment.

A remaining problem with the rapid formation scenario is the previously mentioned discovery by Bensby et al. (2010a; 2011) of a significant number of young ($\sim$3–4 Gyr) and relatively metal–rich bulge dwarfs. This contrasts with the [La/Eu] data presented here and in the literature that seem to rule out a chemical enrichment timescale (and thus age spread) of several Gyr. At the moment there is no obvious solution to this problem, but it could be possible that all previous analyses of bulge RGB stars have selectively chosen targets belonging to the dominant old population. Much larger sample sizes, [La/Eu] determinations for the young and old bulge dwarf populations, and a better understanding of the r–process at solar and super–solar metallicities are clearly needed.

4.2. Comparison to the Halo, Thick Disk, and Thin Disk

4.2.1. The Light Elements

In Figures 13–14 we plot dwarf and giant [Na/Fe], [Al/Fe], and [Na/Al] abundances as a function of [Fe/H] for the Plaut field, Galactic halo, thick disk, and thin disk. The halo and disk data are compiled from the literature, and we have checked to ensure that the abundance ratios from different studies are in agreement, on average. While we generally find very good agreement between the different studies without applying any corrections, the [Al/Fe] ratios for stars with [Fe/H]$<$–0.4 in the Edvardsson et al. (1993) data set were systematically increased by +0.1 dex to match the other literature sources. Since there may be non–negligible systematic differences between abundance ratios derived from dwarfs and giants, in Figure 13 and subsequent figures we differentiate between dwarf and giant data for comparison. As can be seen in Figures 13–14, the giant and dwarf [Na/Fe], [Al/Fe], and [Na/Al] abundances typically agree to within $\sim\pm$0.1 dex, on average.

Although a handful of thick disk stars at [Fe/H]$<$–0.8 have [Na/Fe]$<$0, a majority of the data points scatter between $+0.0\lesssim$[Na/Fe]$\lesssim+0.2$. In contrast, nearly all of the similar metallicity halo stars fall in the range $-0.6\lesssim$[Na/Fe]$\lesssim+0.2$. Therefore, our limited data seem to suggest that the most metal–poor stars in Plaut's field exhibit more halo–like [Na/Fe] ratios, and may be distinctly different from the most metal–poor thick disk stars. If confirmed

in additional fields, the observation that outer bulge abundance ratios are more similar to the halo and inner bulge abundances more similar to the thick disk would be evidence of non–negligible composition differences in the early bulge. However, we note that very few Na abundance measurements are available for low metallicity thick disk giants, which could be important given that NLTE and 3D effects tend to increase in magnitude with decreasing metallicity (e.g., Asplund 2005). On the other hand, the average [Na/Fe] difference between the low metallicity Plaut field giant and thick disk dwarf stars is ∼0.3–0.4 dex, which is significantly larger than the roughly 0.1–0.15 dex NLTE correction predicted for cool, metal–poor giants using the subordinate 6154/6160 Na I lines (e.g., see Lind et al. 2011, their Figure 4).

While the [Na/Fe] differences between the inner and outer bulge disappear at [Fe/H]$\gtrsim$–0.4 (see Figures 8–9), it is clear from Figure 13 that the thick disk and Plaut field differentiate at [Fe/H]>–0.2 (although they are roughly similar in the range –0.6$\lesssim$[Fe/H]$\lesssim$–0.2). On average, the Plaut field stars are more enhanced in [Na/Fe] and continue a trend of increasing [Na/Fe] with [Fe/H]. In contrast, the thick (and thin) disk giant and dwarf data peak in [Na/Fe] at [Fe/H]∼–0.6 and then gradually decline at solar and super–solar metallicities. Interestingly, the thin disk data show an increase in [Na/Fe] at [Fe/H]>0 that brings the bulge and thin disk populations into modest agreement for the most metal–rich stars.

An interesting question is whether the larger star–to–star scatter in the Plaut field compared to disk data has any significance. Although our bulge data and those from the literature share similar dispersions, this may be an artifact of the larger uncertainties associated with analyzing bulge, as opposed to local disk, stars. However, in Figure 15 we overplot two Plaut field giants of similar T_{eff}, log(g), and [Fe/H] but different [Na/Fe]. Note that the Na line strength differences indicate that at least part of our measured [Na/Fe] scatter is real. We note also that Melendez et al. (2008) and Alves–Brito et al. (2010) measured bulge, halo, and disk stars using the same analysis techniques and found comparable star–to–star scatter among all of the populations. We also find that the possible inner disk red clump stars in our sample tend to follow the same [Na/Fe] pattern as the metal–rich thin and thick disk, albeit with larger scatter, which is consistent with the findings by Bensby et al. (2010b) that inner and local disk stars have similar chemical compositions.

Unlike the case for Na, the Plaut field [Al/Fe] abundances closely follow the same trend as the halo and thick disk at all metallicities, and remain $\gtrsim$0.1 dex more enhanced than the thin disk until [Fe/H]>0. We note also that for especially the thick disk there appears to be a roughly 0.1 dex offset between the literature disk and giant [Al/Fe] ratios, and the Plaut field abundances more closely follow those of the literature giant than dwarf trend. Since the halo and metal–poor thick disk share nearly indistinguishable [Al/Fe] abundances, it is

not surprising that there is a similar degree of agreement between the different bulge fields. The similarity in [Al/Fe] (but not [Na/Fe]) between these different populations supports our proposed scenario in which the halo more strongly influenced the initial composition of the outer bulge while the thick disk more strongly influenced the inner bulge. As mentioned in §4.1.1 and seen in Figures 8–9, the Plaut field and bulge dwarf data indicate a downturn in [Al/Fe] and follow the thick disk trend, but the other bulge literature abundances suggest that [Al/Fe] remains significantly enhanced. Unfortunately, adding the thin/thick disk data to this picture does not help solve the [Al/Fe] discrepancy at high metallicities. Finally, in a similar fashion to the [Na/Fe] abundances, the [Al/Fe] ratios of the Plaut field clump stars once again follow the thin/thick disk distribution.

The origin of the three low [Na/Fe] and [Al/Fe] stars is not immediately clear. We note that the stars are near the lower envelope of the halo [Na/Fe] and [Al/Fe] distributions, but it seems unlikely that three randomly chosen halo stars at [Fe/H]$\sim$–1 would all have [Na/Fe]$\lesssim$–0.5 and [Al/Fe]$\lesssim$–0.2. Alternatively, one or all of these stars could have formed in the first generation of a now disrupted or tidally stripped globular cluster. While first generation globular cluster stars are low in both [Na/Fe] and [Al/Fe], very few of these stars have [Al/Fe]<–0.1 and none really reach [Al/Fe]$\lesssim$–0.2 (e.g., Carretta et al. 2009). Interestingly, two of the stars have [La/Eu]$\approx$–0.30, which is consistent with the other bulge stars, the halo, and globular clusters. However, the other star (2MASS 18182256–3401248) has [La/Eu]$\approx$+0.10, which suggests it may have a different origin than the other two low Na and Al stars. While some dwarf galaxies also host stars with low [Na/Fe] and [Al/Fe] and enhanced [La/Eu] ratios (e.g., see review by Venn et al. 2004 and references therein), the enhanced [α/Fe] ratios for these three stars makes a dwarf galaxy origin unlikely.

The [Na/Al] plots in Figure 14 further suggest that there may be key composition differences between the thick disk and outer bulge. For stars with [Fe/H]$\lesssim$–0.8, the [Na/Al] ratios of the Plaut field are clearly lower than both the thick disk dwarf and giant data, and instead are more similar to those of the halo. While there could be systematic differences affecting our data that could shift the points into better agreement with both the halo and thick disk, that is unlikely to flatten the [Na/Al] slope (though we note that the rise in [Na/Al] is greater for the thick disk dwarf compared to giant data). In contrast, the metal–poor inner bulge data from Figures 8–9 are a better match to the thick disk. At higher metallicities ([Fe/H]$\gtrsim$–0.2), the Plaut field data clearly extend to larger [Na/Al] ratios than the average thin or thick disk star, but the inner disk red clump stars generally follow the thick disk trend. Interestingly, the shape of the [Na/Al] distribution may be sensitive to the stellar population. In particular, the thin disk exhibits essentially no change in [Na/Al] as a function of metallicity, the thick disk and halo show steeper positive slopes, and the Plaut field has the steepest positive slope. This may be a result of increasing Na/Al yields

in massive stars, with faster star formation and chemical enrichment producing a steeper relation versus iron. It would be interesting if that were the case because the [Na/Al] ratio would be tracing a different timescale than the [La/Eu] ratio, which we have shown in Figure 12 as being identical at b=–4° and b=–8°.

4.2.2. The Heavy Elements

In Figure 16 we plot [Zr/Fe] and [La/Fe] as a function of [Fe/H] for the Plaut field, halo, thick, and thin disk. While there is a global trend of decreasing [Zr/Fe] abundance with increasing [Fe/H], the various populations do not exhibit significantly different [Zr/Fe] trends. This follows the results shown in Figure 11, which indicate that the light neutron–capture element [Y/Fe] and [Zr/Fe] trends are nearly indistinguishable at different bulge locations. Similarly, the inner disk clump stars also exhibit little variation with [Fe/H] and agree with the thin and thick disk trends. However, the halo stars at [Fe/H]$\lesssim$–1 tend to have [Zr/Fe]$\gtrsim$+0.1, on average, while the most metal–poor Plaut field stars have [Zr/Fe]$\sim$+0.00. Given the small number of bulge [Zr/Fe] measurements at [Fe/H]<–1 and the larger errors associated with the measured [Zr/Fe] ratios, it is difficult to determine whether this reflects a real difference. Several of the bulge stars near [Fe/H]$\sim$–0.8 exhibit [Zr/Fe] enhancements that match the highest halo and thick disk values.

While there is some ambiguity regarding the [Zr/Fe] (and [Y/Fe]) trends, the [La/Fe] distribution provides better differentiation among the various populations. On average, the halo exhibits [La/Fe]>+0.00, but most of the thin and thick disk stars lie at [La/Fe]$\leq$+0.00. Figure 16 shows that the most metal–poor Plaut field bulge giants are at least 0.1–0.2 dex more La–enhanced than the thick disk and are instead much more similar to the halo composition. Although the bulge [La/Fe] values overlap with the thick disk stars between –1.0$\lesssim$[Fe/H]$\lesssim$–0.6, the bulge stars with [Fe/H]>–0.6 are at least 0.1–0.3 dex lower than many of the thin and thick disk stars. However, this discrepancy is smaller for the Baade's window data and may only be present at the 0.1–0.2 dex level. While the [La/Fe] trend for the thick disk slowly declines as a function of increasing [Fe/H], the bulge fields exhibit a sharper decline in [La/Fe] at [Fe/H]>–0.8. In contrast, the inner disk clump stars once again exhibit large star–to–star abundance variations, but their [La/Fe] ratios are roughly similar to the thin and thick disk, on average.

In Figure 17 we plot [Eu/Fe] and [La/Eu] as a function of [Fe/H] for Plaut's field and the halo, thick disk, and thin disk. As was mentioned in §4.1.2, the [Eu/Fe] distributions are indistinguishable between the halo, thick disk, and bulge for metallicities at which they overlap. While the thin disk appears to also exhibit a similar [Eu/Fe] distribution, this

is mostly a consequence of mixing results from the literature. Individual, self–consistent studies (e.g., Bensby et al. 2005) tend to find that the thin disk stars are under–abundant in [Eu/Fe], relative to the thick disk, by at least 0.1 dex, and we find that the bulge [Eu/Fe] distribution is more similar to the halo and thick disk than the thin disk. We have also taken the position that the decrease in [Eu/Fe] at [Fe/H]$\sim$–0.4, at least for the bulge, is more a reflection of the metallicity dependent yields and singular production source (core–collapse SNe) of Eu than an indicator of Fe production from Type Ia SNe (see also McWilliam et al. 2010).

As the right panels of Figure 17 indicate, the halo and disk data form a trend of slowly increasing [La/Eu] ratios with increasing metallicity. This contrasts with the generally flat [La/Eu] trends for the Plaut and Baade's window giants (see also Figure 12), but we note that a large portion of the bulge and thick disk [La/Eu] data overlap. In the metallicity range over which the bulge and thin disk overlap, the thin disk [La/Eu] ratios are, on average, at least 0.2 dex higher than the bulge values. The enhanced [La/Eu] ratios for the inner disk clump stars seem compatible with this trend. We interpret this as evidence that the main s–process played a much larger role in especially the thin disk's chemical enrichment compared to the bulge. In comparison with the halo and thick disk, the enhanced [La/Eu] ratios in many of the metal–poor Plaut (and Baade's window) stars is not clear. Only a small percentage of halo and thick disk stars at [Fe/H]$\lesssim$–1 have [La/Eu]>–0.20. Therefore, we would not expect to find such a large percentage of bulge stars in our limited sample to have [La/Eu]>–0.20, if the bulge formed from a mixture of halo and thick disk gas. A larger sample of metal–poor bulge stars is needed to further address this issue.

5. SUMMARY

We have determined chemical abundances of Na, Al, Zr, La, Nd, and Eu for 39 RGB stars and an additional 23 potential red clump inner disk stars in Plaut's low extinction window. We have also measured Li in one of the stars that was identified as being super Li–rich. The abundances were measured from high resolution (R$\approx$25,000), high S/N ($\sim$50–100 pixel^{-1}) spectra obtained with the Hydra multifiber spectrograph on the CTIO Blanco 4m telescope. The [Fe/H], [Si/Fe], and [Ca/Fe] abundances and the model atmosphere parameters were taken from the first paper in this series (Johnson et al. 2011). We developed a new computationally parallel version of the spectrum synthesis module for MOOG, and employed this code to derive all abundances presented here.

At the metal–poor end, we find that the bulge RGB stars in Plaut's field have [Na/Fe]$\sim$–0.30 and [Al/Fe]$\sim$+0.20. However, the [Na/Fe] ratios increase with metallicity and reach a

maximum of [Na/Fe]$\sim$+0.30 at [Fe/H]$\sim$–0.20. The [Na/Fe] trend flattens out and remains enhanced to higher metallicities. In contrast, the [Al/Fe] trend is nearly identical to that of [α/Fe]. In particular, the [Al/Fe] ratio remains relatively flat and at [Al/Fe]$\sim$+0.2 until [Fe/H]$\sim$–0.20, at which point there is a downturn in [Al/Fe] toward solar values. Additionally, we do not find evidence supporting a significant [Na/Fe]–[Al/Fe] correlation for the bulge, as is found in most globular clusters. However, three metal–poor stars in our sample exhibit anomalously low [Na/Fe] and [Al/Fe] ratios. Two of the stars have Na, Al, and heavy element abundance patterns that indicate a possible origin as first generation globular cluster stars. The other star shows an enhanced [La/Eu] ratio that is generally inconsistent with the r–process dominant composition of globular clusters. Although the inner disk clump stars generally exhibit larger star–to–star abundance dispersions, presumably because of larger distance uncertainties, we find that they tend to share a similar [Al/Fe] trend with the bulge giants but have lower [Na/Fe] ratios, on average.

The single super Li–rich giant (log ϵ(Li)=+3.51) discovered in our sample does not appear to exhibit any other unusual spectroscopic features. While it has [Al/Fe] and [Eu/Fe] abundances that are slightly below average, these values are well within the envelope of measurements for the other bulge giants. The [La/Fe] and [Nd/Fe] ratios for this star are very consistent with similar metallicity stars. By combining this star with other super Li–rich bulge giants found in the literature, we estimate that the fraction of super Li–rich RGB stars in the bulge is $\sim$1%. This is similar to what is found in the disk and globular clusters.

The light neutron–capture element Zr exhibits a trend of slightly decreasing [Zr/Fe] with increasing metallicity. Interestingly, in the range –0.8$\lesssim$[Fe/H]$\lesssim$–0.4, roughly a third of the sample have [Zr/Fe]$\gtrsim$+0.1. We speculate that these stars may have been systematically enriched by the weak s– and/or r–processes compared to the majority of bulge stars that have [Zr/Fe]$\lesssim$+0.00. For the heavier neutron–capture elements La and Nd, the most metal–poor bulge stars are enhanced at [La,Nd/Fe]$\sim$+0.2 with very little star–to–star scatter; however, both elements exhibit decreasing trends for [Fe/H]>–0.8. The La and Nd distributions decline until reaching [La,Nd/Fe]$\sim$–0.3 in the highest metallicity stars. The inner disk clump stars appear to be more enhanced in both La and Nd than the bulge giants.

The [Eu/Fe] abundance distribution for the bulge stars (and the clump stars at higher metallicity) directly follows that of the [Al/Fe] and [α/Fe] trends. Eu is enhanced at [Eu/Fe]$\sim$+0.3 dex until [Fe/H]$\sim$–0.2, at which point the [Eu/Fe] trend declines toward solar and sub–solar values. When we examine the [La/Eu] ratio as a function of metallicity, we find that all but the most metal–poor bulge stars have [La/Eu]$\sim$–0.3. This suggests that the Plaut field bulge stars formed rapidly and before the main s–process could become a significant pollution source. The more enhanced [La/Eu] ratios in some of the most metal–

poor stars is intriguing, and may be a chemical tag indicating pre–enrichment of the early bulge gas. Interestingly, the clump stars exhibit noticeably higher [La/Eu] ratios than the similar metallicity bulge giants, which suggests these stars formed over a longer timescale.

In addition to analyzing the abundance trends of the Plaut field stars, we also compared our results with those from the literature spanning various bulge locations. We generally find good agreement between the abundance trends in different fields, and also between the dwarfs and giants. In particular, we find the following trends to be "universal" among all bulge studies: (1) increasing [Na/Fe] with [Fe/H], (2) enhanced [Al/Fe], (3) a rising [Na/Al] ratio with [Fe/H], (4) a mostly flat [Zr/Fe] (or [Y/Fe]) trend with a small percentage of Zr/Y–enhanced stars, (5) a trend of decreasing [La/Fe] (or [Ba/Fe]) with increasing metallicity, (6) an α–like distribution of [Eu/Fe], and (7) a flat distribution at [La/Eu]$\sim$–0.3 with some enhancements at the metal–poor end. Interestingly, stars in both the b=–4° and b=–8° fields exhibit identical [La/Eu] distributions that seem to rule out the main s–process, which operates on long timescales, as a significant pollution source. This result appears to conflict with the observation of a non–negligible population of young ($\sim$3–4 Gyr old) microlensed dwarfs in the bulge.

Despite the general agreement, for Na there is some evidence that the metal–poor ([Fe/H]$\lesssim$–0.8) inner bulge stars may be 0.1–0.3 dex more enhanced than the outer bulge stars. Interestingly, this difference disappears at [Fe/H]$\gtrsim$–0.8, and we interpret this as a reflection of significant composition inhomogeneities in the early bulge. For Al there is remarkable agreement that [Al/Fe]$\sim$+0.2 from [Fe/H]=–1.5 up to –0.2, but two different abundance trends emerge in the literature at higher metallicities: one set finds that Al remains enhanced at super–solar metallicities and the other set (which includes the present work) finds that Al decreases in abundance like Eu and the α–elements. At the moment there does not seem to be an obvious solution to this problem.

We also compare our derived abundance trends with similar literature data for the Galactic halo, thick disk, and thin disk. While we find in agreement with past studies that the bulge and thick disk share many composition similarities, we also find evidence of significant differences. One of the elements showing the strongest difference between the bulge and thick disk is Na. At the metal–poor end, the Plaut field stars have [Na/Fe] ratios that are at least 0.3 dex lower than similar metallicity thick disk stars, and are instead more similar to those found in the halo. Although there is significant overlap in [Na/Fe] between the thick disk and bulge at higher metallicities, the overall shape of the bulge Na distribution is different and extends to higher values of [Na/Fe]. Additionally, we find that the enhanced [La/Fe] ratios for the metal–poor bulge stars and the steep decline in [La/Fe] with increasing metallicity does not match the thick disk trend. Interestingly, the same is not true for Eu.

The bulge, halo, and thick disk all exhibit nearly identical [Eu/Fe] versus [Fe/H] trends. We interpret this as evidence that the downturn in [Eu/Fe] at [Fe/H]$\sim$–0.4, which is common to the thick disk and bulge, is more a reflection of metallicity dependent r–process yields than a statement of the Type II/Type Ia SN ratio.

CIJ would like to thank David Yong for several useful discussions, and would also like to thank Andrea Kunder, Livia Origlia, Nils Ryde, Elena Valenti, Thomas Bensby, Dave Arnett, and Alvio Renzini for many useful discussions at the Aspen Center for Physics, which is supported by the National Science Foundation under award No. 1066293. We thank Andy McWilliam for many useful discussions and for providing data from McWilliam et al. (2010). We would like to thank David Reitzel for obtaining a portion of these observations. This research has made use of NASA's Astrophysics Data System Bibliographic Services. This material is based upon work supported by the National Science Foundation under award No. AST–1003201 to CIJ and award No. AST–0709479 to RMR.

REFERENCES

Alves-Brito, A., Meléndez, J., Asplund, M., Ramírez, I., & Yong, D. 2010, A&A, 513, A35

Anders, E., & Grevesse, N. 1989, Geochim. Cosmochim. Acta, 53, 197

Andrievsky, S. M., Spite, M., Korotin, S. A., et al. 2008, A&A, 481, 481

Aoki, W., et al. 2001, ApJ, 561, 346

Arcoragi, J.-P., Langer, N., & Arnould, M. 1991, A&A, 249, 134

Arlandini, C., Käppeler, F., Wisshak, K., Gallino, R., Lugaro, M., Busso, M., & Straniero, O. 1999, ApJ, 525, 886

Arnett, W. D., & Thielemann, F.-K. 1985, ApJ, 295, 589

Arnould, M., Goriely, S., & Takahashi, K. 2007, Phys. Rep., 450, 97

Asplund, M. 2005, ARA&A, 43, 481

Asplund, M., Grevesse, N., Sauval, A. J., & Scott, P. 2009, ARA&A, 47, 481

Ballero, S. K., Matteucci, F., Origlia, L., & Rich, R. M. 2007, A&A, 467, 123

Beer, H., & Macklin, R. L. 1985, Phys. Rev. C, 32, 738

Bensby, T., Feltzing, S., & Lundström, I. 2003, A&A, 410, 527

Bensby, T., Feltzing, S., Lundström, I., & Ilyin, I. 2005, A&A, 433, 185

Bensby, T., Feltzing, S., Johnson, J. A., et al. 2010a, A&A, 512, A41

Bensby, T., Alves-Brito, A., Oey, M. S., Yong, D., & Meléndez, J. 2010b, A&A, 516, L13

Bensby, T., Adén, D., Meléndez, J., et al. 2011, A&A, 533, A134

Bisterzo, S., Gallino, R., Straniero, O., Cristallo, S., Kappeler, F. 2010, MNRAS, 404, 1529

Brewer, M.-M., & Carney, B. W. 2006, AJ, 131, 431

Brown, J. A., Sneden, C., Lambert, D. L., & Dutchover, E., Jr. 1989, ApJS, 71, 293

Burris, D. L., Pilachowski, C. A., Armandroff, T. E., Sneden, C., Cowan, J. J., & Roe, H. 2000, ApJ, 544, 302

Busso, M., Gallino, R., & Wasserburg, G. J. 1999, ARA&A, 37, 239

Carretta, E., Bragaglia, A., Gratton, R., & Lucatello, S. 2009, A&A, 505, 139

Chiappini, C., Frischknecht, U., Meynet, G., Hirschi, R., Barbuy, B., Pignatari, M., Decressin, T., & Maeder, A. 2011, Nature, 472, 454

Clarkson, W., Sahu, K., Anderson, J., et al. 2008, ApJ, 684, 1110

Clayton, D. D., & Rassbach, M. E. 1967, ApJ, 148, 69

Cowan, J. J., Thielemann, F.-K., & Truran, J. W. 1991, Phys. Rep., 208, 267

de La Reza, R., Drake, N. A., da Silva, L., Torres, C. A. O., & Martin, E. L. 1997, ApJ, 482, L77

D'Antona, F., & Ventura, P. 2007, MNRAS, 379, 1431

Decressin, T., Meynet, G., Charbonnel, C., Prantzos, N., & Ekström, S. 2007, A&A, 464, 1029

Denisenkov, P. A., & Denisenkova, S. N. 1990, Soviet Astronomy Letters, 16, 275

Den Hartog, E. A., Lawler, J. E., Sneden, C., & Cowan, J. J. 2003, ApJS, 148, 543

Edvardsson, B., Andersen, J., Gustafsson, B., et al. 1993, A&A, 275, 101

Feltzing, S., & Gilmore, G. 2000, A&A, 355, 949

François, P., Depagne, E., Hill, V., et al. 2007, A&A, 476, 935

Freiburghaus, C., Rosswog, S., & Thielemann, F.-K. 1999, ApJ, 525, L121

Fulbright, J. P. 2000, AJ, 120, 1841

Fulbright, J. P., McWilliam, A., & Rich, R. M. 2007, ApJ, 661, 1152

Gallino, R., Arlandini, C., Busso, M., Lugaro, M., Travaglio, C., Straniero, O., Chieffi, A., & Limongi, M. 1998, ApJ, 497, 388

Gehren, T., Liang, Y. C., Shi, J. R., Zhang, H. W., & Zhao, G. 2004, A&A, 413, 1045

Girardi, L., Bressan, A., Bertelli, G., & Chiosi, C. 2000, A&AS, 141, 371

Gonzalez, O. A., Zoccali, M., Monaco, L., et al. 2009, A&A, 508, 289

Gonzalez, O. A., Rejkuba, M., Zoccali, M., et al. 2011, A&A, 530, A54

Gratton, R. G., Carretta, E., Eriksson, K., & Gustafsson, B. 1999, A&A, 350, 955

Gratton, R., Sneden, C., & Carretta, E. 2004, ARA&A, 42, 385

Hanson, R. B., Sneden, C., Kraft, R. P., & Fulbright, J. 1998, AJ, 116, 1286

Herwig, F. 2005, ARA&A, 43, 435

Hill, V., Lecureur, A., Gómez, A., et al. 2011, A&A, 534, A80

Hobbs, L. M., Thorburn, J. A., & Rebull, L. M. 1999, ApJ, 523, 797

Honda, S., Aoki, W., Ishimaru, Y., & Wanajo, S. 2007, ApJ, 666, 1189

Johnson, J. A. 2002, ApJS, 139, 219

Johnson, J. A., & Bolte, M. 2002, ApJ, 579, 616

Johnson, C. I., Rich, R. M., Fulbright, J. P., Valenti, E., & McWilliam, A. 2011, ApJ, 732, 108

Käppeler, F., Beer, H., & Wisshak, K. 1989, Reports on Progress in Physics, 52, 945

Karakas, A. I. 2010, MNRAS, 403, 1413

Kobayashi, C., Umeda, H., Nomoto, K., Tominaga, N., & Ohkubo, T. 2006, ApJ, 653, 1145

Kobayashi, C., Karakas, A. I., & Umeda, H. 2011, MNRAS, 414, 3231

Kraft, R. P., Peterson, R. C., Guhathakurta, P., et al. 1999, ApJ, 518, L53

Kroupa, P. 2008, Pathways Through an Eclectic Universe, 390, 3

Kuijken, K., & Rich, R. M. 2002, AJ, 124, 2054

Kupka, F. G., Ryabchikova, T. A., Piskunov, N. E., Stempels, H. C., & Weiss, W. W. 2000, Baltic Astronomy, 9, 590

Lamb, S. A., Howard, W. M., Truran, J. W., & Iben, I., Jr. 1977, ApJ, 217, 213

Langer, N., Arcoragi, J.-P., & Arnould, M. 1989, A&A, 210, 187

Lattimer, J. M., Mackie, F., Ravenhall, D. G., & Schramm, D. N. 1977, ApJ, 213, 225

Lawler, J. E., Bonvallet, G., & Sneden, C. 2001a, ApJ, 556, 452

Lawler, J. E., Wickliffe, M. E., den Hartog, E. A., & Sneden, C. 2001b, ApJ, 563, 1075

Lebzelter, T., Uttenthaler, S., Busso, M., Schultheis, M., & Aringer, B. 2012, A&A, 538, A36

Lecureur, A., Hill, V., Zoccali, M., et al. 2007, A&A, 465, 799

Lind, K., Asplund, M., & Barklem, P. S. 2009, A&A, 503, 541

Lind, K., Asplund, M., Barklem, P. S., & Belyaev, A. K. 2011, A&A, 528, A103

Mashonkina, L. I., Shimanskiĭ, V. V., & Sakhibullin, N. A. 2000, Astronomy Reports, 44, 790

Mathews, G. J., & Cowan, J. J. 1990, Nature, 345, 491

Matteucci, F., & Recchi, S. 2001, ApJ, 558, 351

McWilliam, A., & Rich, R. M. 1994, ApJS, 91, 749

McWilliam, A., Preston, G. W., Sneden, C., & Searle, L. 1995, AJ, 109, 2757

McWilliam, A. 1998, AJ, 115, 1640

McWilliam, A., Fulbright, J., & Rich, R. M. 2010, IAU Symposium, 265, 279

Meléndez, J., Asplund, M., Alves-Brito, A., et al. 2008, A&A, 484, L21

Nataf, D. M., & Gould, A. P. 2011, arXiv:1112.1072

Nissen, P. E., & Schuster, W. J. 1997, A&A, 326, 751

Ortolani, S., Renzini, A., Gilmozzi, R., et al. 1995, Nature, 377, 701

Peters, J. G. 1968, ApJ, 154, 225

Peterson, R. C., Dalle Ore, C. M., & Kurucz, R. L. 1993, ApJ, 404, 333

Pignatari, M., Gallino, R., Heil, M., Wiescher, M., Käppeler, F., Herwig, F., & Bisterzo, S. 2010, ApJ, 710, 1557

Prantzos, N., Arnould, M., & Arcoragi, J.-P. 1987, ApJ, 315, 209

Prantzos, N., Hashimoto, M., & Nomoto, K. 1990, A&A, 234, 211

Press, W. H., Teukolsky, S. A., Vetterling, W. T., & Flannery, B. P. 1992, Cambridge: University Press, —c1992, 2nd ed.

Prochaska, J. X., Naumov, S. O., Carney, B. W., McWilliam, A., & Wolfe, A. M. 2000, AJ, 120, 2513

Raiteri, C. M., Busso, M., Picchio, G., Gallino, R., & Pulone, L. 1991a, ApJ, 367, 228

Raiteri, C. M., Busso, M., Picchio, G., & Gallino, R. 1991b, ApJ, 371, 665

Raiteri, C. M., Gallino, R., Busso, M., Neuberger, D., & Kaeppeler, F. 1993, ApJ, 419, 207

Rangwala, N., Williams, T. B., & Stanek, K. Z. 2009, ApJ, 691, 1387

Raskin, C., Scannapieco, E., Rhoads, J., & Della Valle, M. 2009, ApJ, 707, 74

Reddy, B. E., Tomkin, J., Lambert, D. L., & Allende Prieto, C. 2003, MNRAS, 340, 304

Reddy, B. E., Lambert, D. L., & Allende Prieto, C. 2006, MNRAS, 367, 1329

Ruchti, G. R., Fulbright, J. P., Wyse, R. F. G., et al. 2011, ApJ, 743, 107

Ryan, S. G., Norris, J. E., & Beers, T. C. 1996, ApJ, 471, 254

Shen, J., Rich, R. M., Kormendy, J., et al. 2010, ApJ, 720, L72

Simmerer, J., Sneden, C., Cowan, J. J., et al. 2004, ApJ, 617, 1091

Sneden, C. 1973, ApJ, 184, 839

Sneden, C., Cowan, J. J., & Gallino, R. 2008, ARA&A, 46, 241

Stephens, A., & Boesgaard, A. M. 2002, AJ, 123, 1647

Straniero, O., Gallino, R., & Cristallo, S. 2006, Nuclear Physics A, 777, 311

Sweigart, A. V., & Mengel, J. G. 1979, ApJ, 229, 624

Takahashi, K., Witti, J., & Janka, H.-T. 1994, A&A, 286, 857

The, L.-S., El Eid, M. F., & Meyer, B. S. 2007, ApJ, 655, 1058

Thielemann, F. K., & Arnett, W. D. 1985, ApJ, 295, 604

Tinsley, B. M. 1979, ApJ, 229, 1046

Travaglio, C., Gallino, R., Arnone, E., et al. 2004, ApJ, 601, 864

Truran, J. W. 1981, A&A, 97, 391

Truran, J. W., Cowan, J. J., Pilachowski, C. A., & Sneden, C. 2002, PASP, 114, 1293

Venn, K. A., Irwin, M., Shetrone, M. D., et al. 2004, AJ, 128, 1177

Ventura, P., & D'Antona, F. 2009, A&A, 499, 835

Vieira, K., Casetti-Dinescu, D. I., Méndez, R. A., et al. 2007, AJ, 134, 1432

Woosley, S. E., Wilson, J. R., Mathews, G. J., Hoffman, R. D., & Meyer, B. S. 1994, ApJ, 433, 229

Woosley, S. E., & Weaver, T. A. 1995, ApJS, 101, 181

Yong, D., Lambert, D. L., Paulson, D. B., & Carney, B. W. 2008, ApJ, 673, 854

Yoshii, Y., Tsujimoto, T., & Nomoto, K. 1996, ApJ, 462, 266

Zoccali, M., Renzini, A., Ortolani, S., et al. 2003, A&A, 399, 931

Zoccali, M., Hill, V., Lecureur, A., et al. 2008, A&A, 486, 177

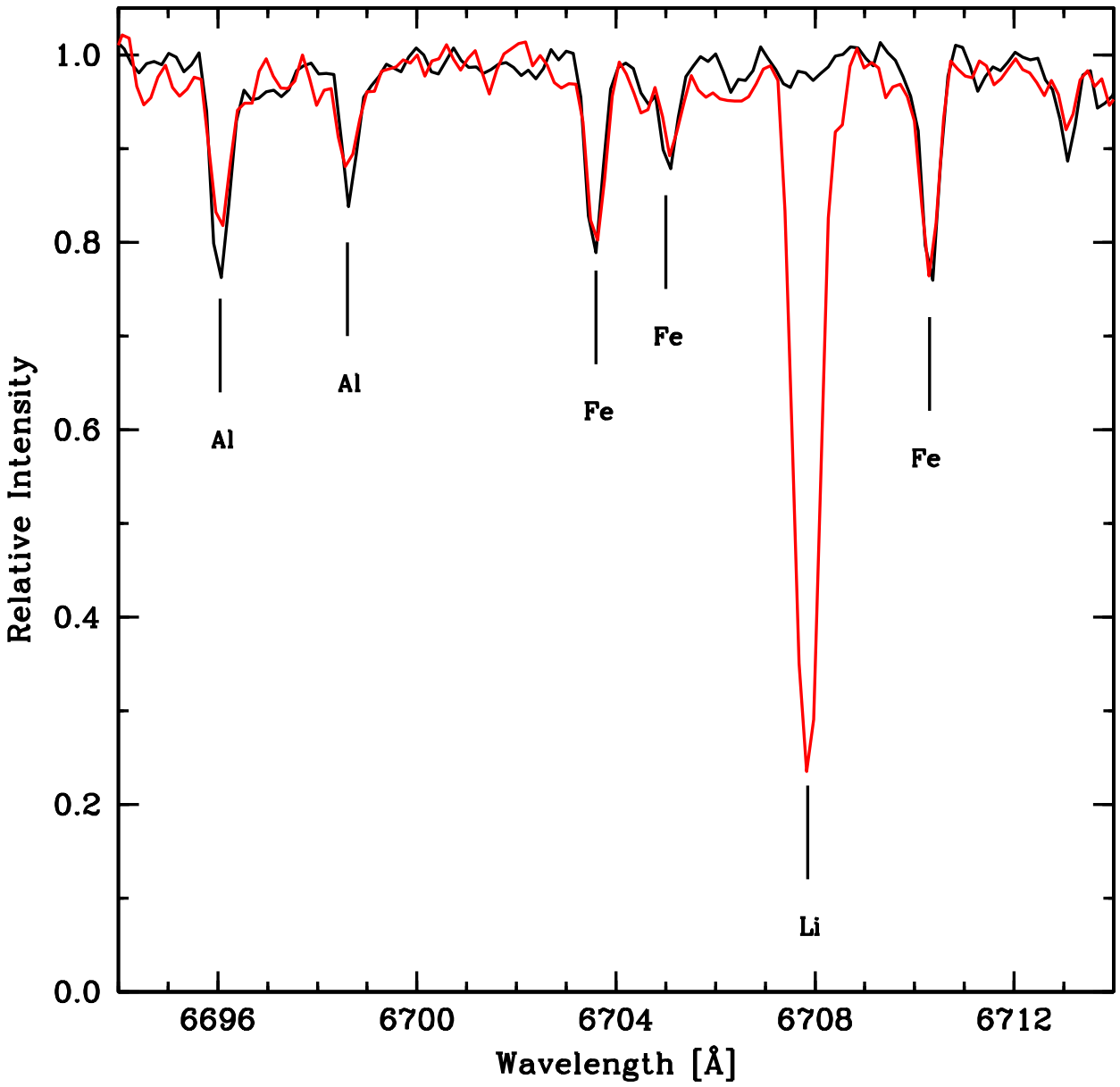

Fig. 1.— This figure illustrates the line strength difference between the Li–rich giant 2MASS 18183679–3251454 (solid red line) and a similar "Li–normal" giant 2MASS 18181929–3404128 (solid black line). Both stars have nearly identical temperatures, surface gravities, and metallicities, but the Li lines are drastically different. Note also the line strength differences in the two Al lines.

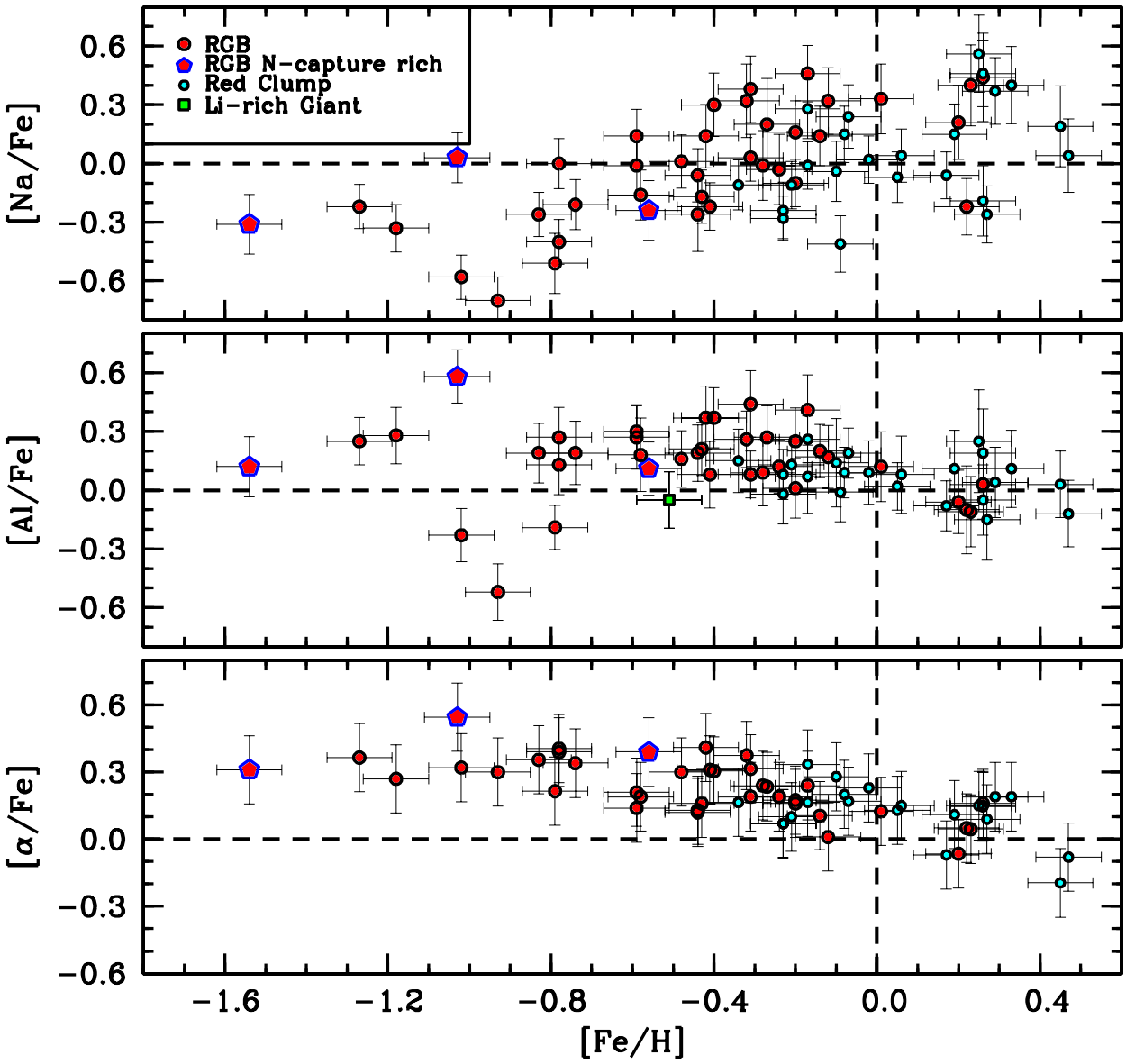

Fig. 2.— Plots of [Na/Fe], [Al/Fe], and [α/Fe] are shown as a function of [Fe/H]. The [α/Fe] abundances are from Johnson et al. (2011) and [α/Fe] is defined as $\frac{1}{2}$([Si/Fe]+[Ca/Fe]). The red filled circles are the bulge RGB stars, and the filled cyan circles are the foreground red clump stars in our sample. The blue outlined pentagons are the stars with anomalously high neutron–capture element abundances, and the filled green box is the Li–rich giant.

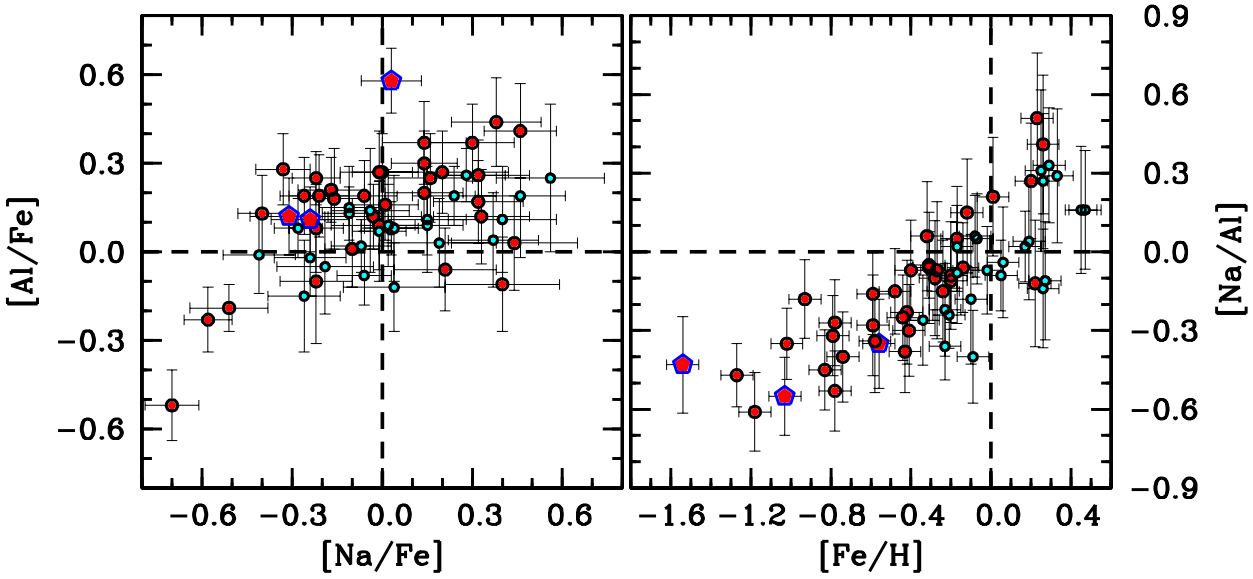

Fig. 3.— The left panel shows [Na/Fe] vs [Al/Fe] for all stars in our sample. The right panel illustrates the change in the [Na/Al] ratio as a function of [Fe/H]. The symbols are the same as those in Figure 2.

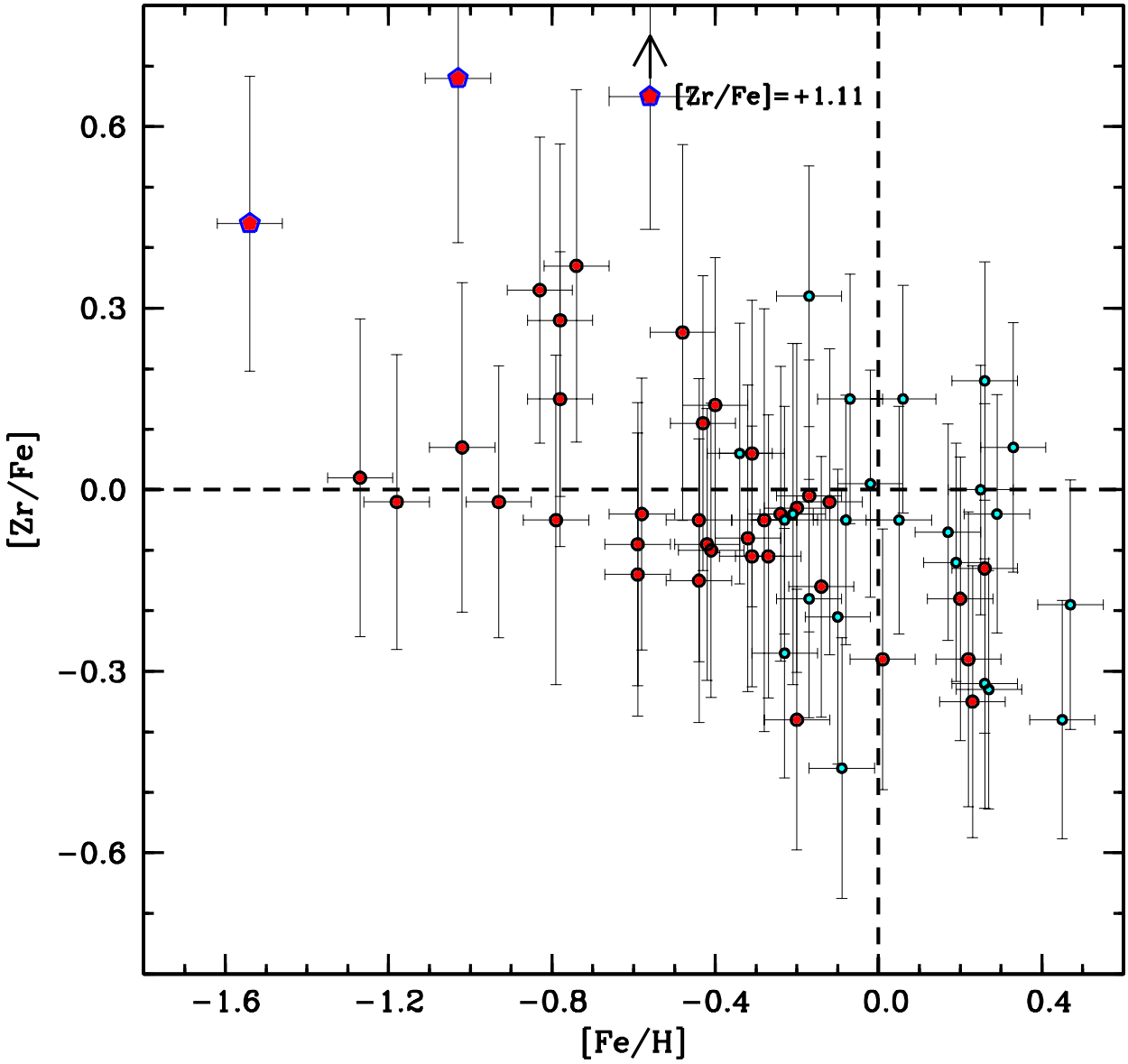

Fig. 4.— The [Zr/Fe] ratios are plotted as a function of [Fe/H]. The symbols are the same as those in Figure 2.

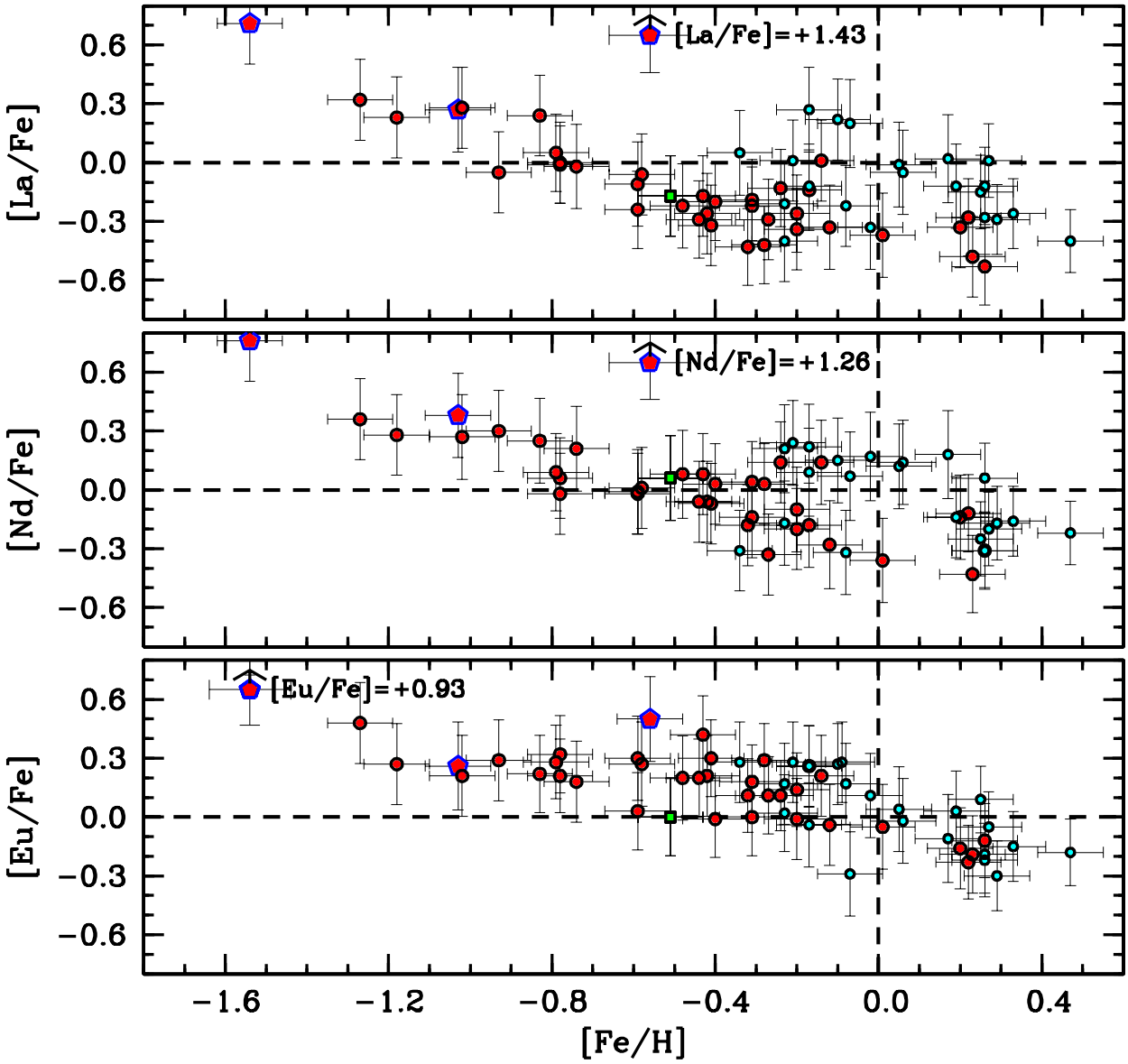

Fig. 5.— [La/Fe], [Nd/Fe], and [Eu/Fe] are plotted as a function of [Fe/H]. The symbols are the same as those in Figure 2.

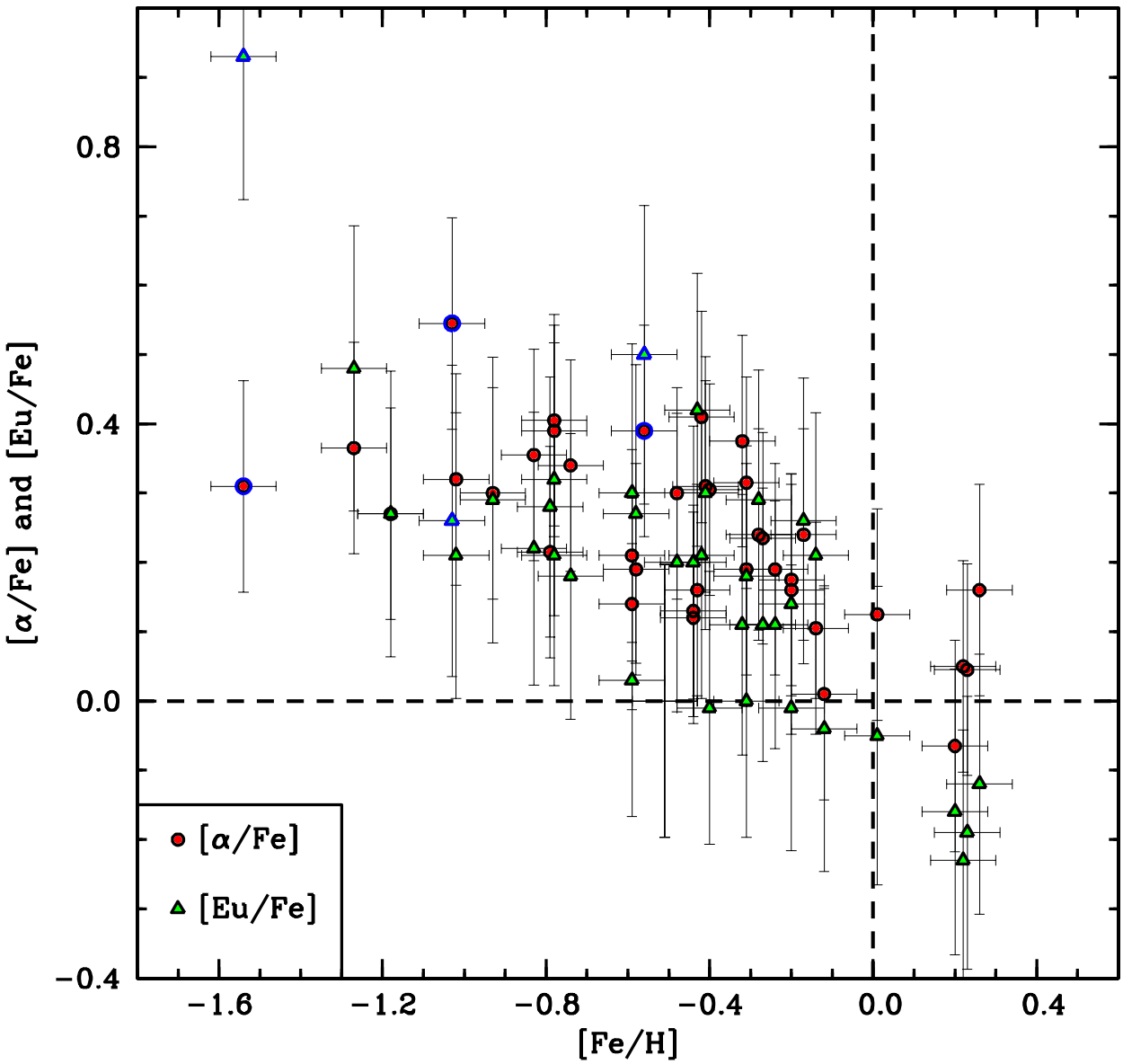

Fig. 6.— [α/Fe] (filled red circles) and [Eu/Fe] (filled green triangles) are plotted as a function of [Fe/H]. Note that the objects plotted here are only the bulge RGB stars, and the blue outlined points are the same as those in Figures 2–5.

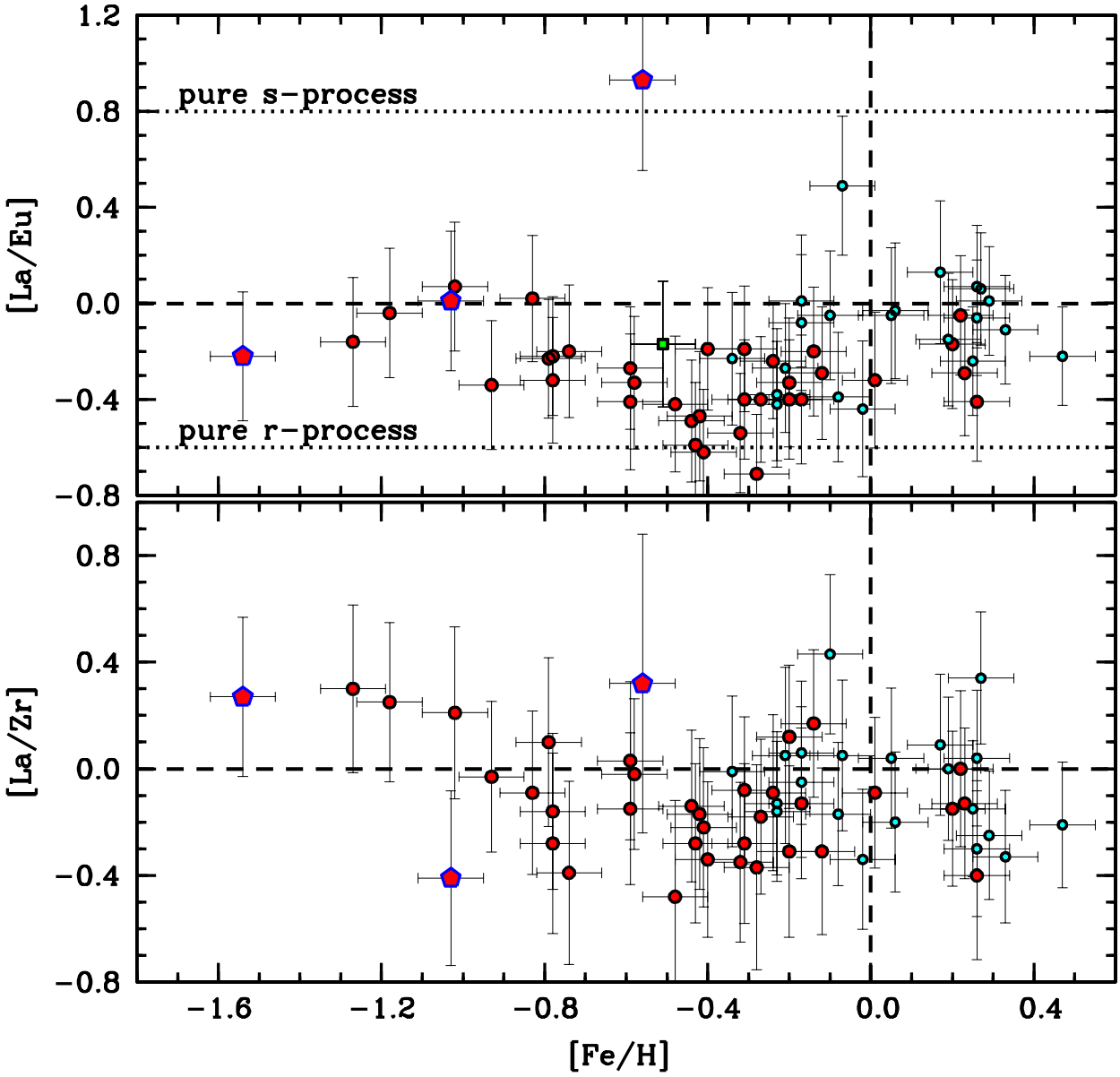

Fig. 7.— [La/Eu] and [La/Zr] are plotted as a function of [Fe/H]. The symbols are the same as those in Figure 2. The dotted lines in the left panel indicate the abundance ratios expected for pure r– and s–process enrichment by Kappeler et al. (1989) and the "standard pocket" model of Bisterzo et al. (2010), respectively.

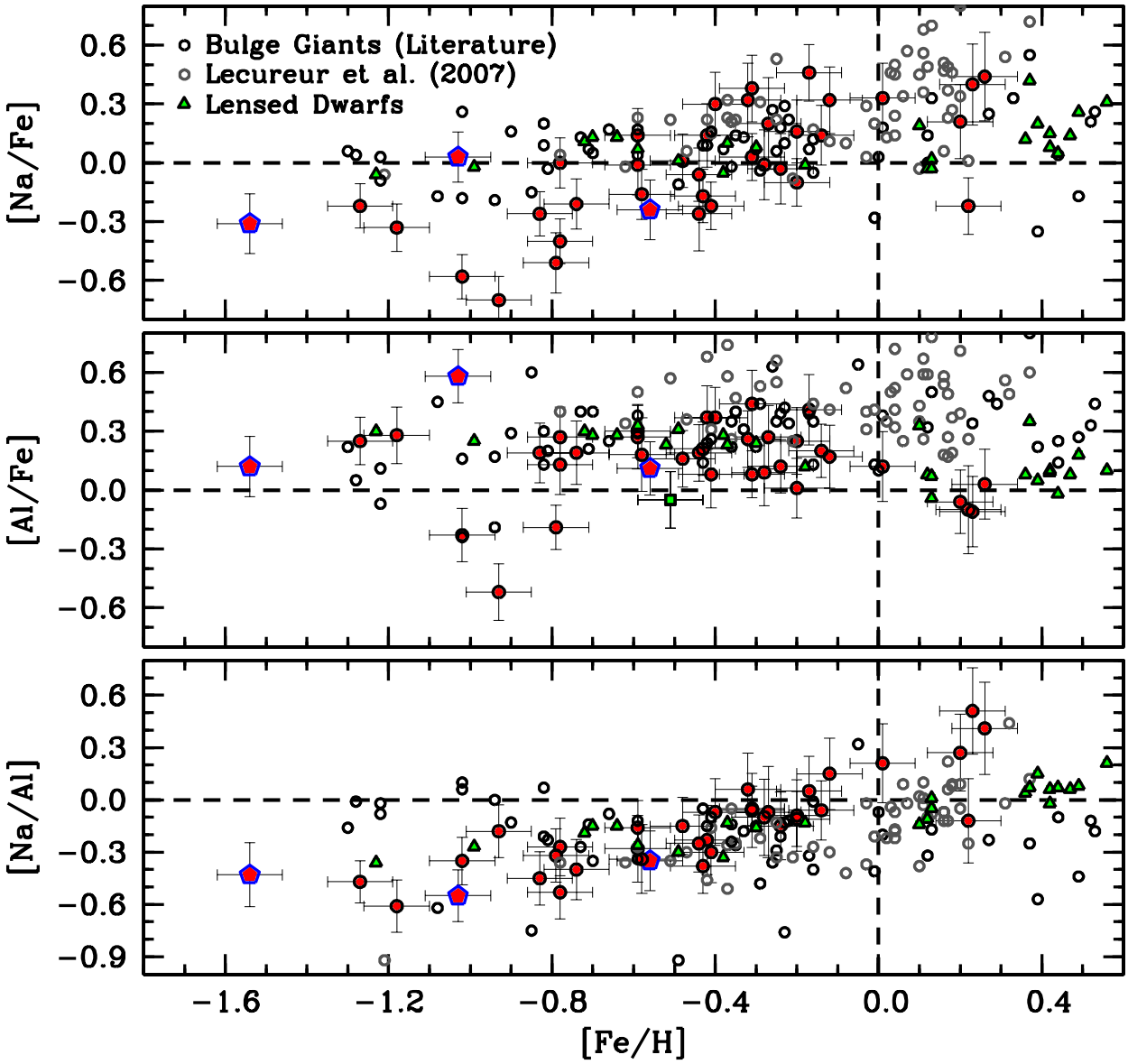

Fig. 8.— [Na/Fe], [Al/Fe], and [Na/Al] plotted as a function of [Fe/H] for bulge stars only. The symbols for our data are the same as those in Figure 2. The open black circles represent bulge RGB data from McWilliam & Rich (1994), Fulbright et al. (2007), and Alves–Brito et al. (2010). The open grey circles are the bulge RGB data from Lecureur et al. (2007), and the filled green triangles are from the microlensed dwarf studies by Bensby et al. (2010a; 2011).

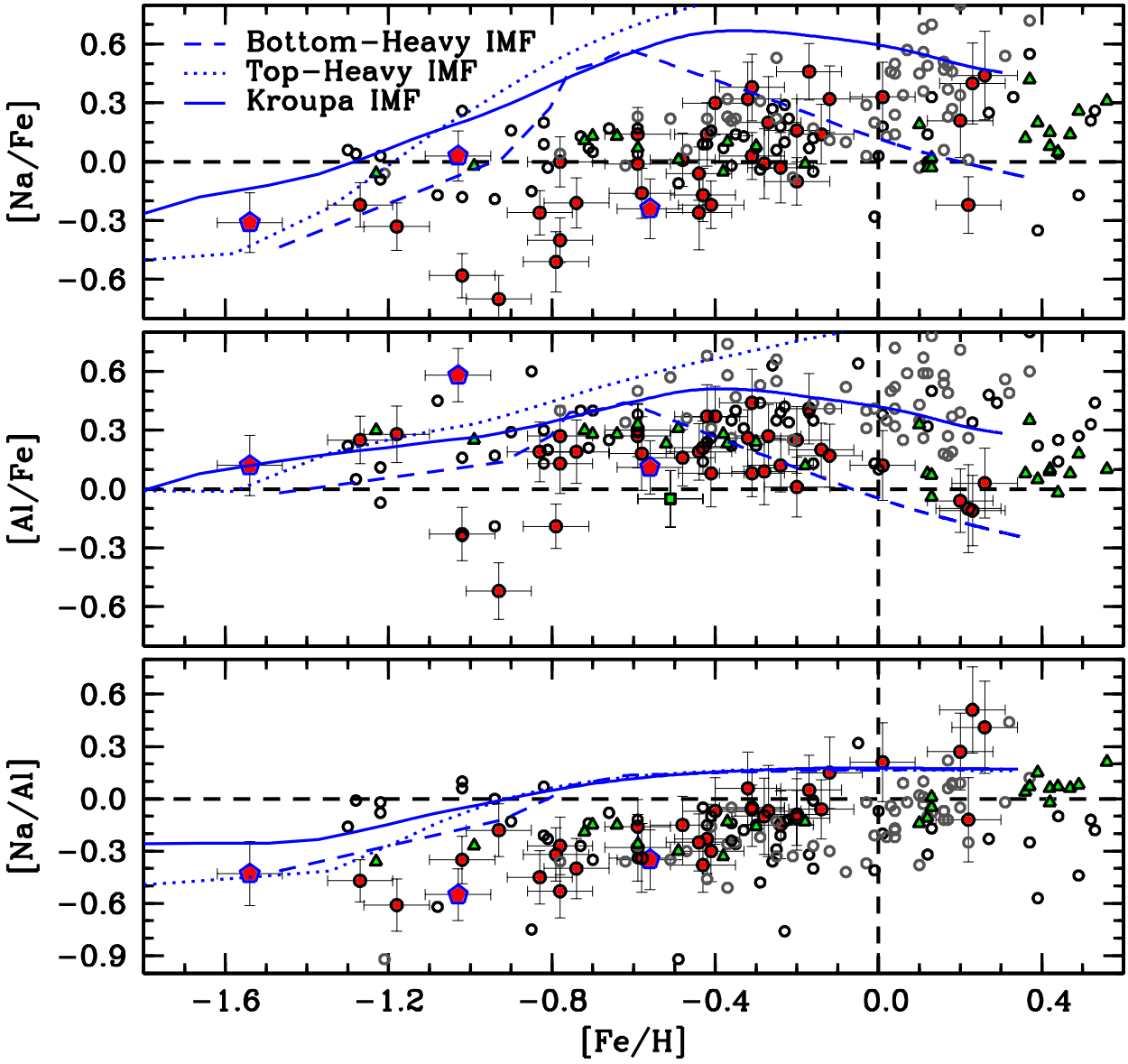

Fig. 9.— The same plot as Figure 8 with bulge chemical enrichment models of varying IMF overplotted. The models follow the prescriptions outlined in Kobayashi et al. (2006; 2010; see also §4 for more details). The solid blue lines illustrate the models based on a Kroupa IMF (x=1.3; Kroupa 2008), the dotted blue lines indicate models based on an extreme top–heavy IMF (x=0.3), and the dashed blue lines indicate models based on an extreme bottom–heavy IMF (x=1.6). Note that Ballero et al. (2007) find an IMF slope x$\leq$0.95 with a high star formation efficiency to best fit the bulge.

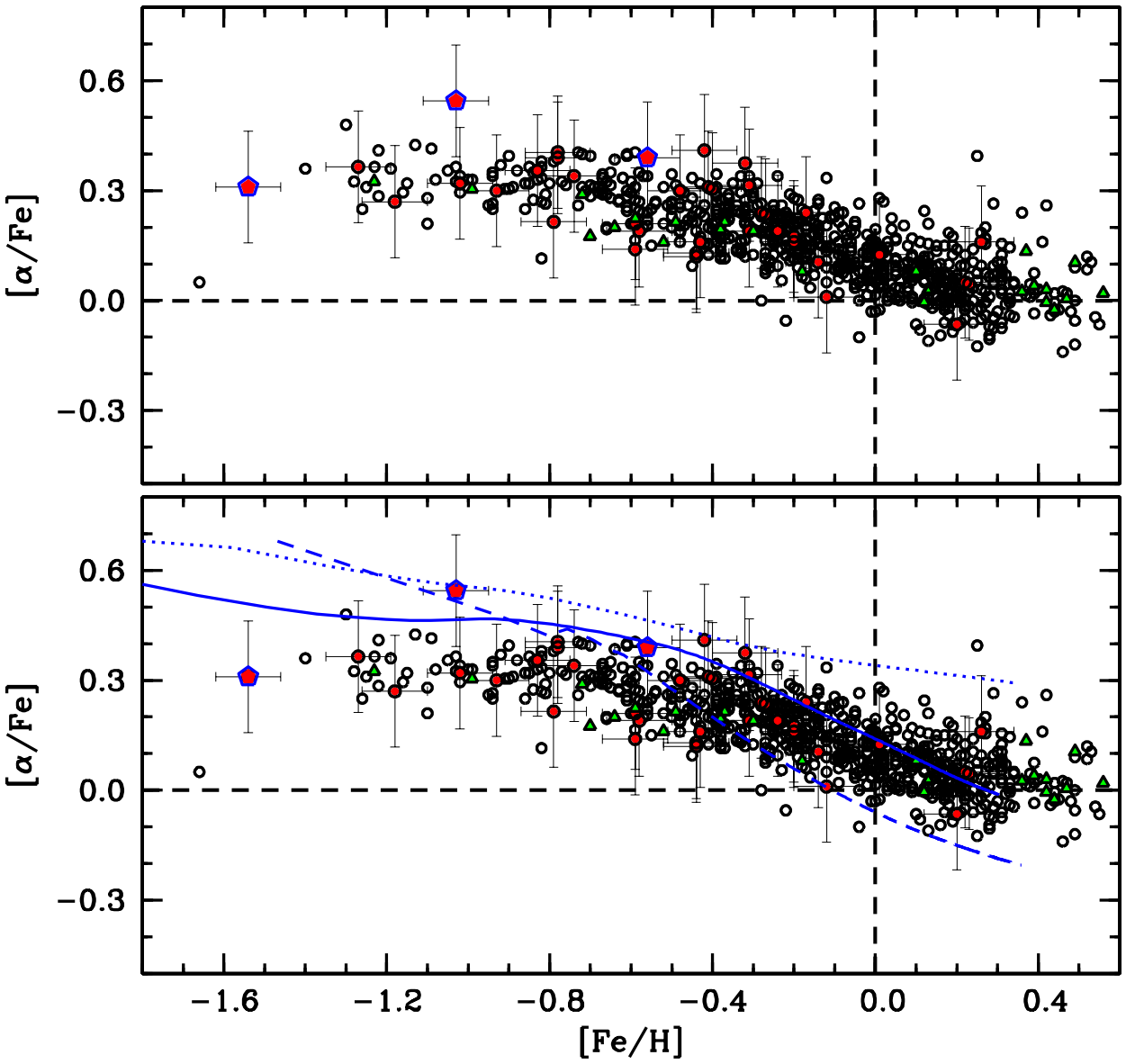

Fig. 10.— Similar to Figures 8–9, the [α/Fe] ratio is plotted as a function of [Fe/H] for bulge RGB and dwarf stars. The symbols are the same as those in Figure 8, and [α/Fe] is defined as $\frac{1}{2}$([Si/Fe]+[Ca/Fe]). The literature RGB data are from McWilliam & Rich (1994), Fulbright et al. (2007), Alves–Brito et al. (2010), Johnson et al. (2011), and Gonzalez et al. (2011). The microlensed dwarf data are from Bensby et al. (2010a; 2011). The bottom panel contains the same data as the top panel, but with the same bulge chemical enrichment models from Figure 9 overplotted.

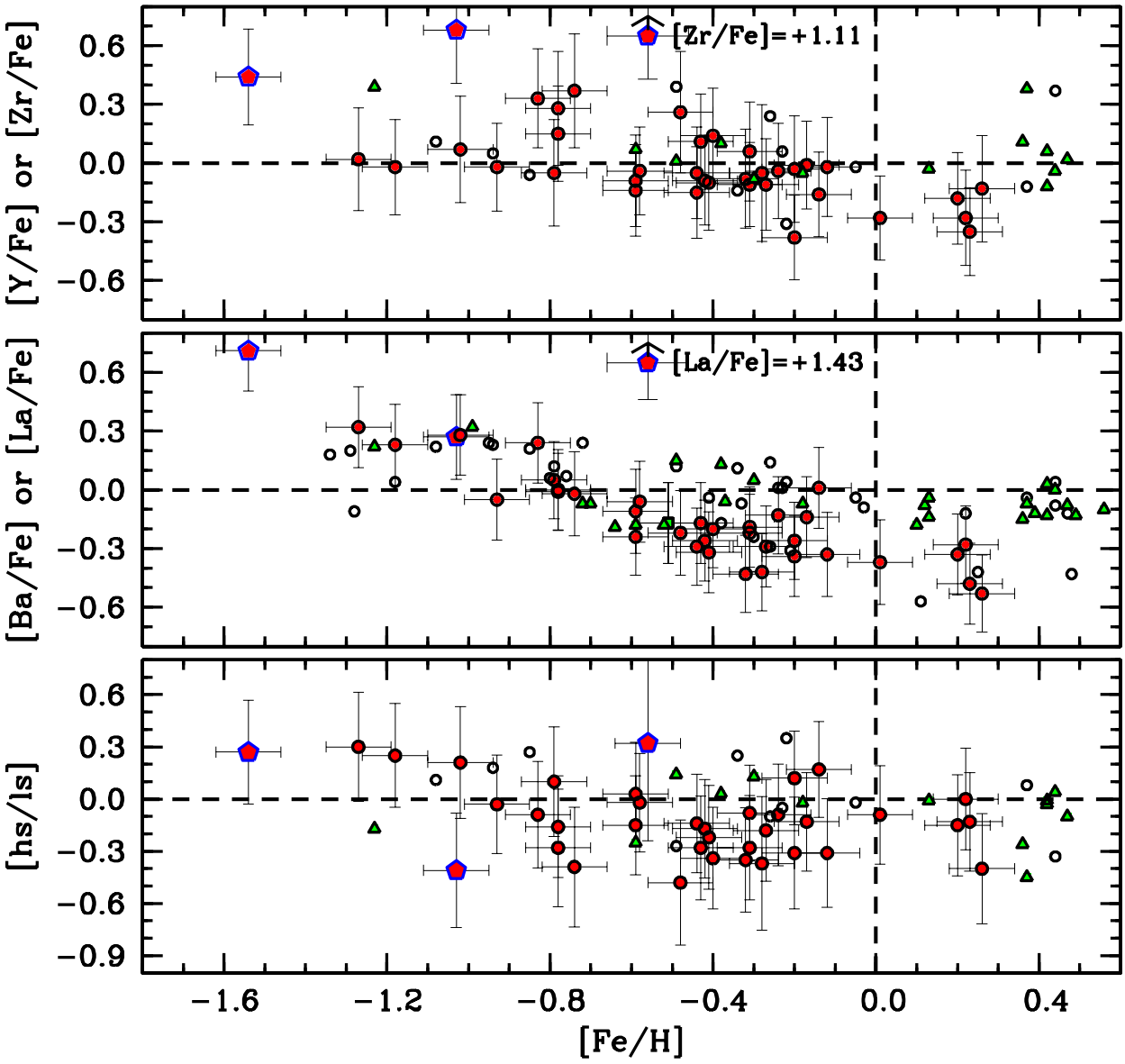

Fig. 11.— The top panel shows the abundance trends of [Y/Fe] (literature data) or [Zr/Fe] (our data) as a function of [Fe/H]. The symbols are the same as those in Figures 2 and 8. The literature data are from Bensby et al. (2010a; 2011) for the dwarfs and McWilliam & Rich (1994) for the giants. The middle panel plots [Ba/Fe] or [La/Fe] as a function of [Fe/H]. [Ba/Fe] data are shown for Bensby et al. (2010a; 2011) and [La/Fe] data are shown for our data, McWilliam & Rich (1994), and McWilliam et al. (2010). The bottom panel plots the "heavy–to–light" neutron–capture ratio ([hs/ls], where heavy is defined as either [Ba/Fe] or [La/Fe] and light is defined as either [Y/Fe] or [Zr/Fe]), as a function of [Fe/H]. The literature data are from Bensby et al. (2010a; 2011) and McWilliam & Rich (1994).

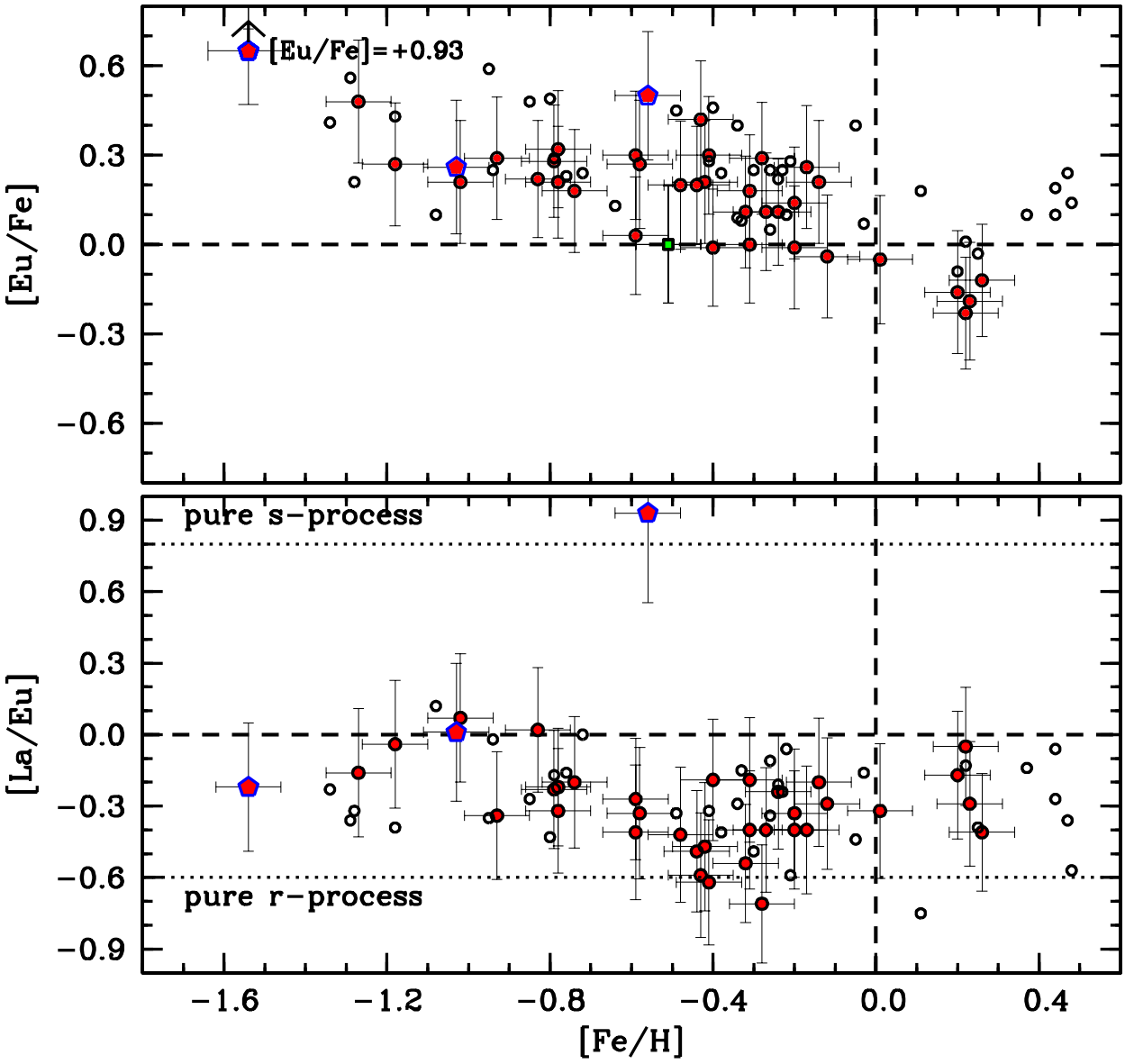

Fig. 12.— In the top panel the [Eu/Fe] ratio is plotted as a function of [Fe/H]. The symbols are the same as those in Figure 8. The literature data are from McWilliam & Rich (1994) and McWilliam et al. (2010). The bottom panel shows the [La/Eu] ratio as a function of [Fe/H], using our data set along with the McWilliam & Rich (1994) and McWilliam et al. (2010) data. The pure r– and s–process lines are the same as those in Figure 7.

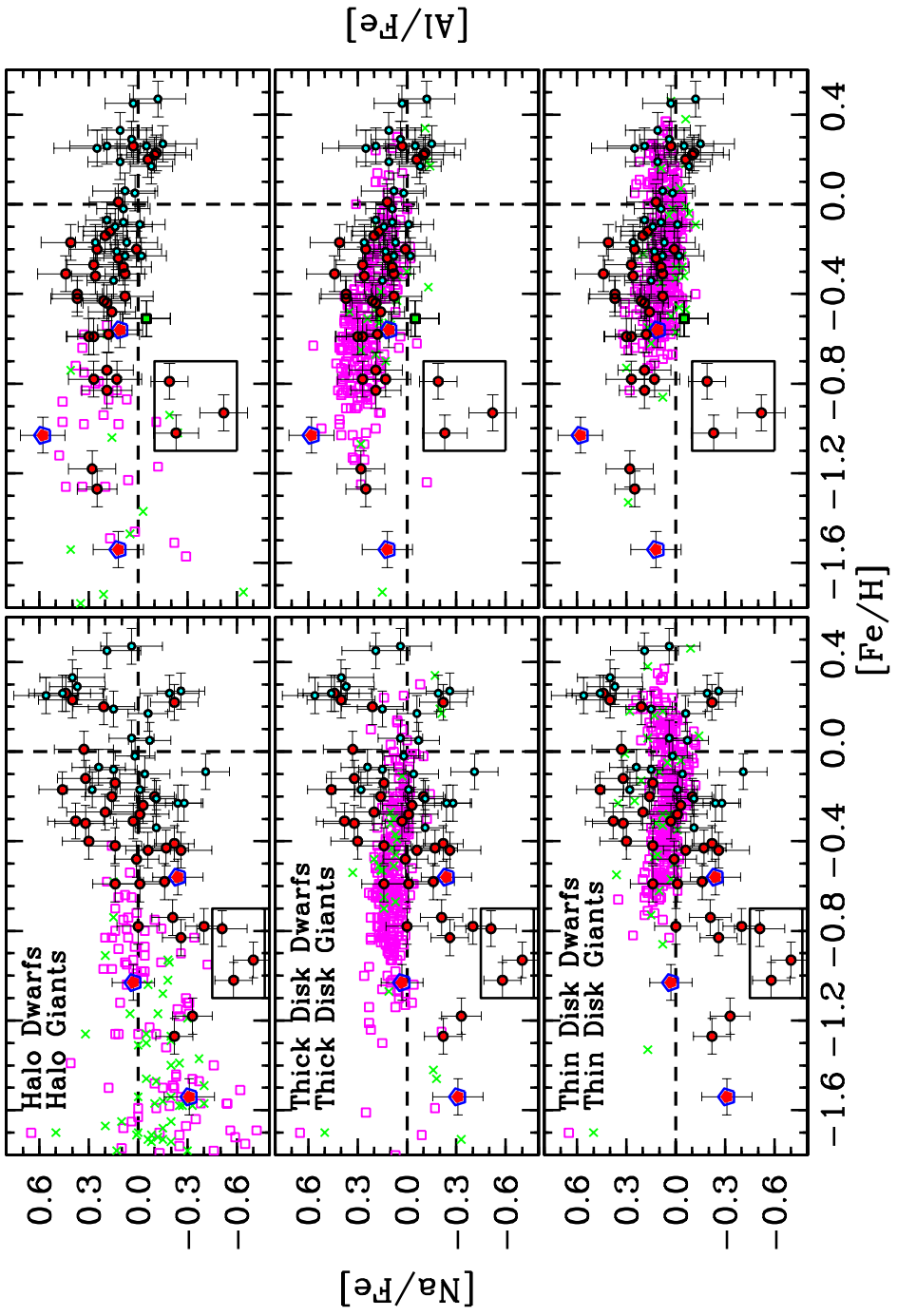

Fig. 13.— [Na/Fe] and [Al/Fe] are plotted as a function of [Fe/H] for our sample and the literature. The red, cyan, and blue outlined symbols are the same as those in Figure 2, and a box has been placed around the three low Na/Al stars for guidance. The magenta open boxes represent literature dwarf abundances for the halo (top panels), thick disk (middle panels), and thin disk (bottom panels). Similarly, the green crosses represent literature giant abundances. The halo data are from McWilliam et al. (1995), Ryan et al. (1996), Nissen & Schuster (1997), Hanson et al. (1998), Fulbright (2000), Johnson (2002), Stephens & Boesgaard (2002), Reddy et al. (2006), and Alves–Brito et al. (2010). The thin and thick disk data are from Edvardsson et al. (1993), Nissen & Schuster (1997), Hanson et al. (1998), Fulbright (2000), Prochaska et al. (2000), Stephens & Boesgaard (2002), Bensby et

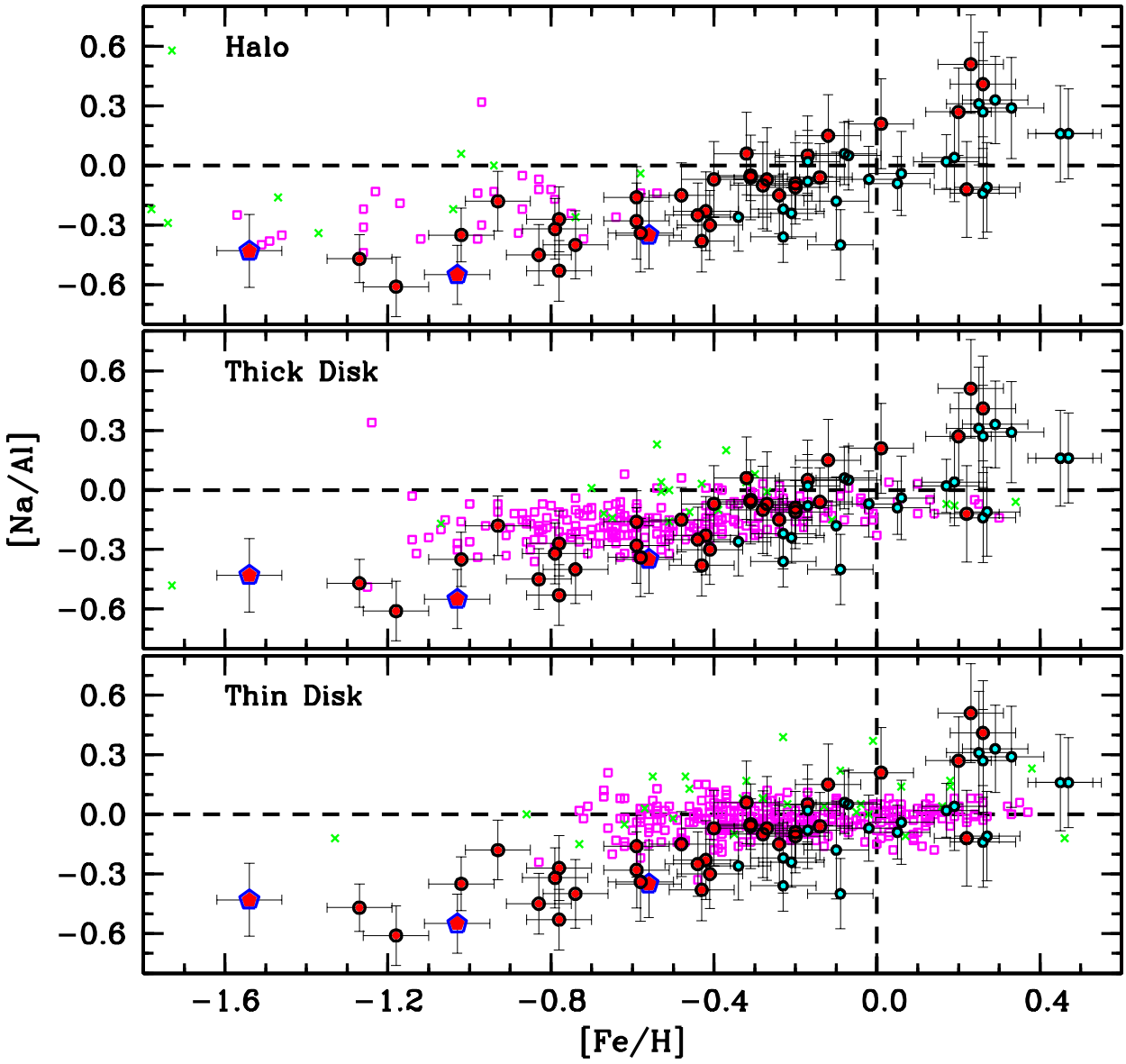

Fig. 14.— A similar plot to Figure 13 comparing our bulge [Na/Al] abundances as a function of [Fe/H] to the halo, thick disk, and thin disk.

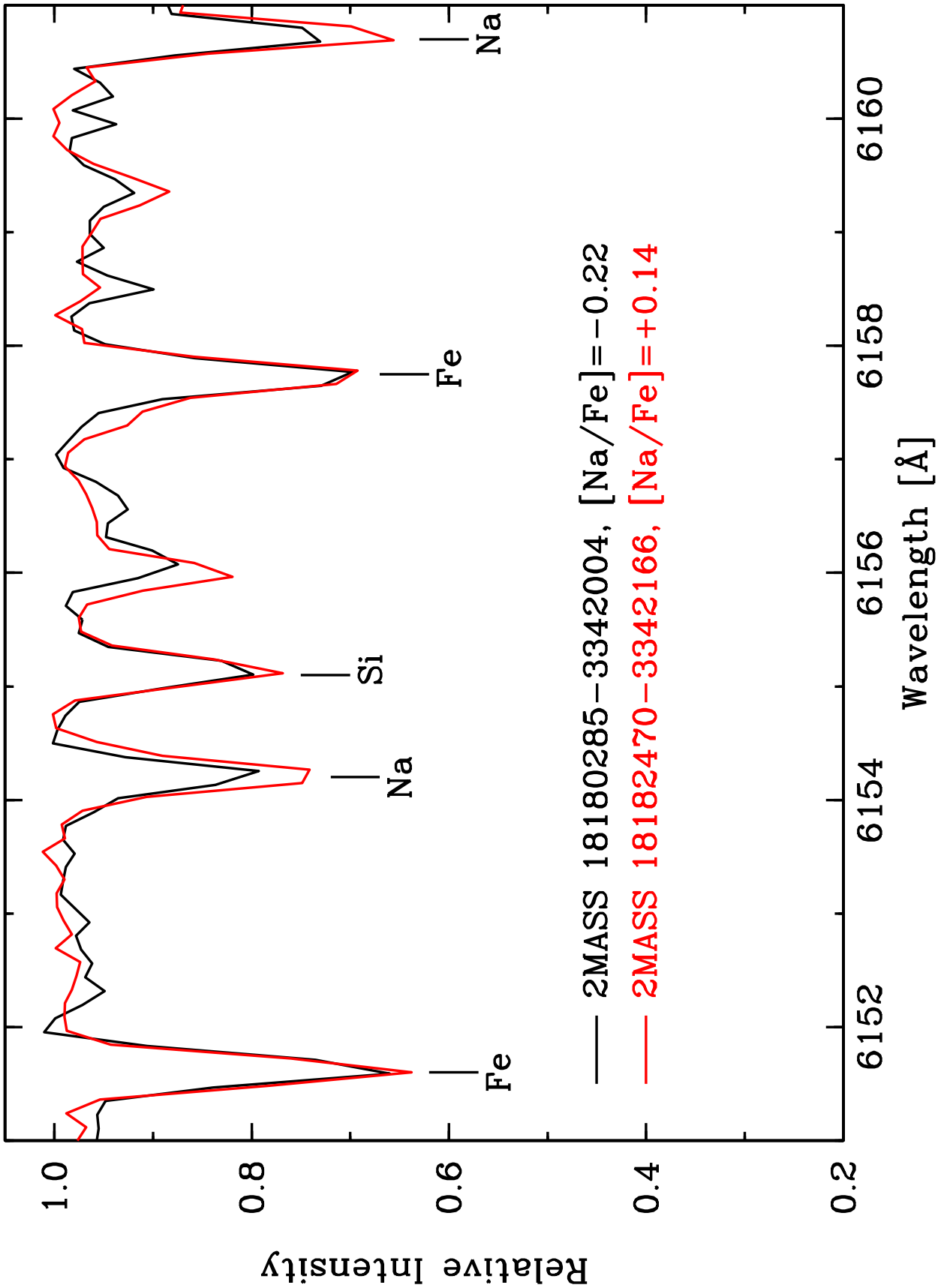

Fig. 15.— Two Plaut field giants of similar temperature, gravity, and metallicity (T_{eff}≈4150 K, log(g)≈1.25 (cgs), and [Fe/H]≈–0.40) but different [Na/Fe] abundances are overplotted.

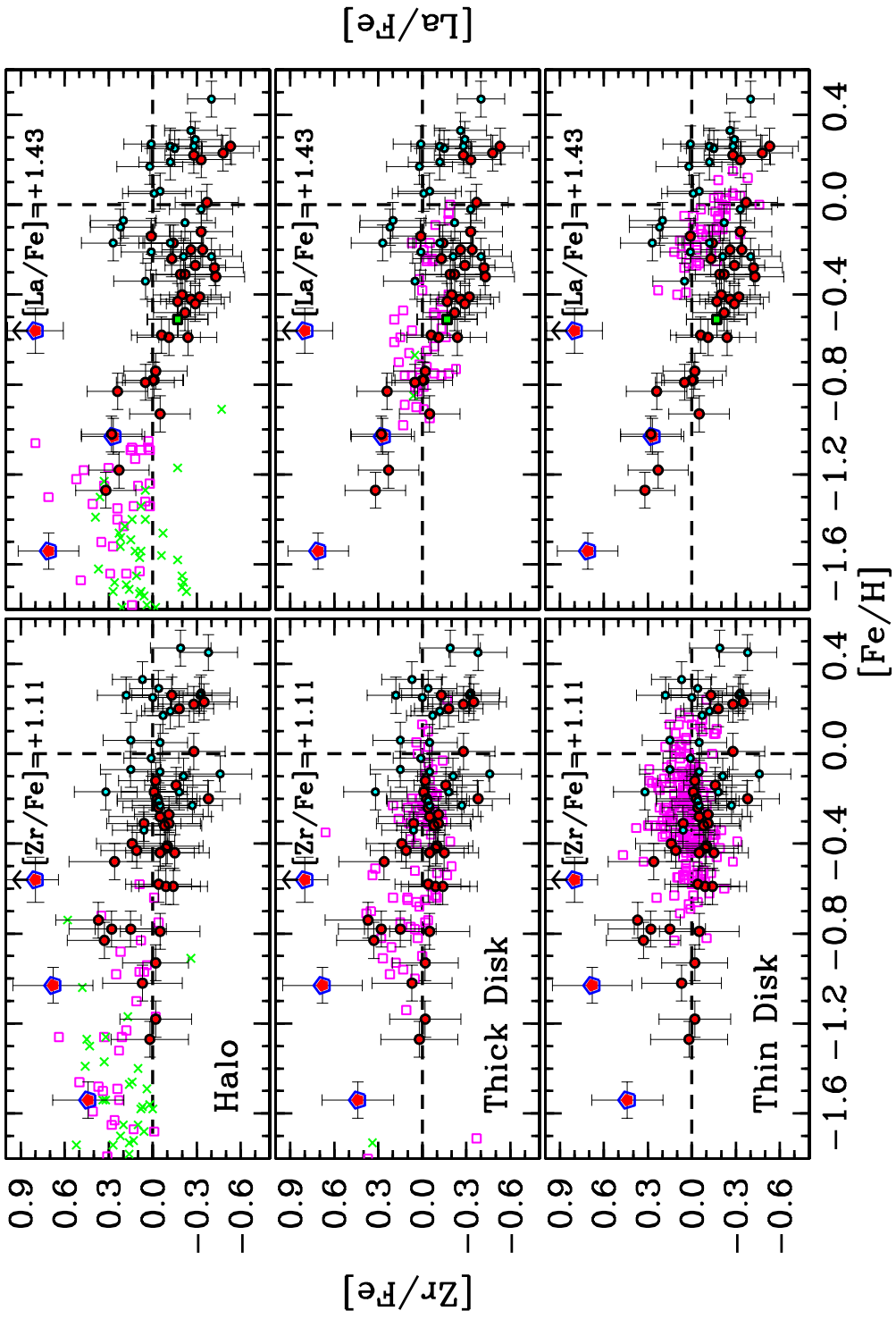

Fig. 16.— Literature [Zr/Fe] and [La/Fe] data are plotted as a function of [Fe/H] in comparison with our bulge results. The symbols are the same as those in Figure 13. The halo data are from McWilliam et al. (1995), Ryan et al. (1996), Fulbright (2000), Johnson (2002), and Simmerer et al. (2004). The thin and thick disk data are from Edvardsson et al. (1993), Reddy et al. (2003), and Brewer & Carney (2006).

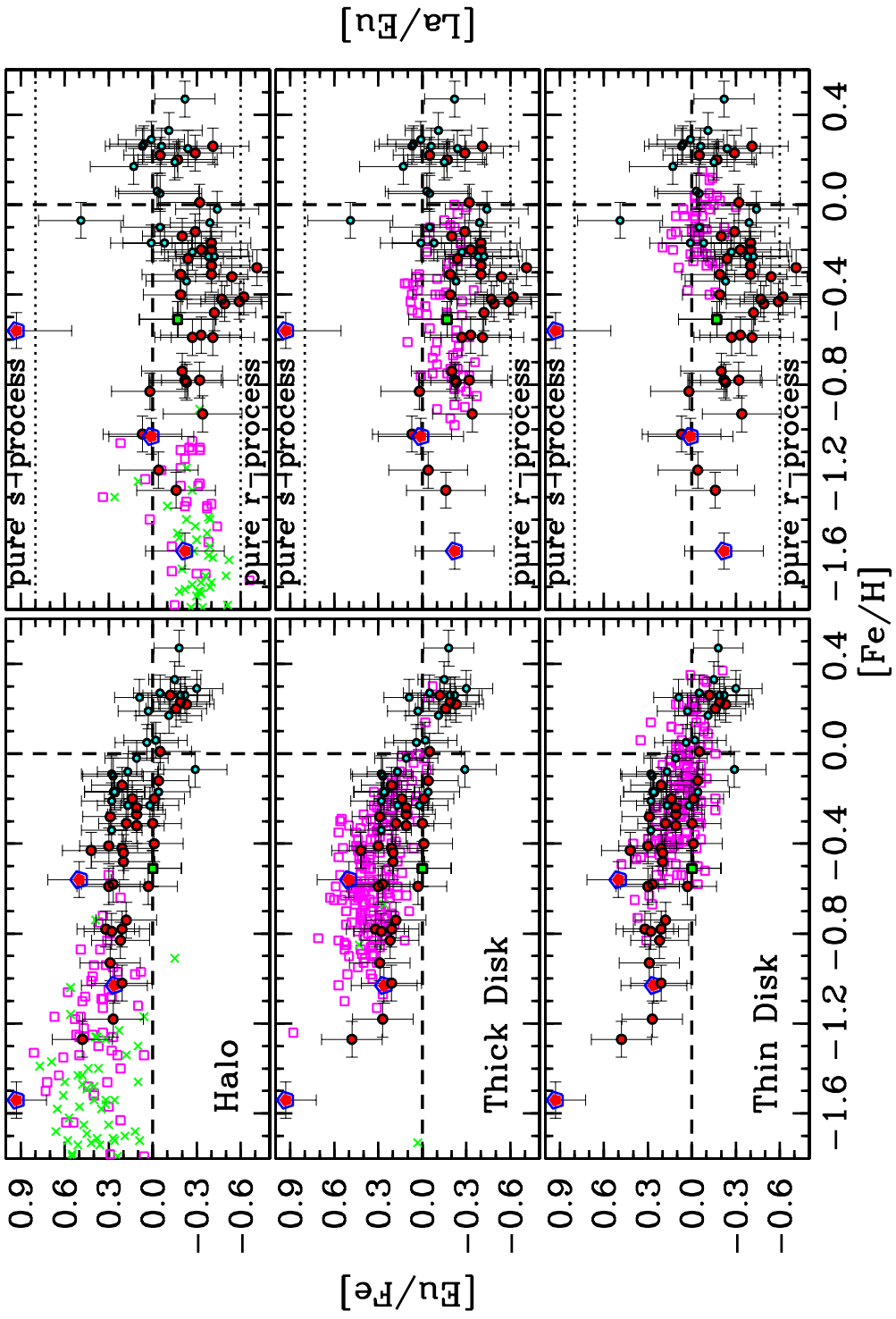

Fig. 17.— Literature [Eu/Fe] and [La/Eu] data are plotted as a function of [Fe/H] in comparison with our bulge results. The symbols are the same as those in Figure 13. The halo data are from McWilliam et al. (1995), Ryan et al. (1996), Fulbright (2000), Johnson (2002), Simmerer et al. (2004), and Reddy et al. (2006). The thin and thick disk data are from Prochaska et al. (2000), Reddy et al. (2003), Bensby et al. (2005), and Brewer & Carney (2006).

Table 1. Linelist and Reference Arcturus Abundances

Element	Wavelength (Å)	E.P. (eV)	log gf	[X/Fe] Arcturus[a]
Li I	6707.768	0.000	+0.17[b]	···
Na I	6154.226	2.101	−1.55	+0.09
Na I	6160.747	2.103	−1.17	+0.09
Al I	6696.023	3.140	−1.57	+0.38
Al I	6698.673	3.140	−1.96	+0.38
Zr I	6134.545	0.000	−1.34	+0.00
Zr I	6140.450	0.519	−1.50	+0.00
Zr I	6143.200	0.071	−1.20	+0.00
La II	6262.290	0.403	−1.22[b]	−0.06
Nd II	6740.078	0.060	−1.77	+0.05
Eu II	6645.060	1.379	+0.12[b]	+0.29

[a]The assumed Arcturus iron abundance is [Fe/H]=–0.50.

[b]The numbers listed represent the total log gf values for each line. The individual components can be found in Hobbs et al. (1999) for Li, Lawler et al. (2001a) for La, and Lawler et al. (2001b) for Eu. Note that the total log gf value for Li listed above only includes the ^{7}Li lines in Hobbs et al. (1999).

Table 2. Model Atmosphere Parameters and Abundance Ratios

Star 2MASS	T_{eff} (K)	log g (cgs)	[Fe/H]	V_t (km s^{-1})	[Na/Fe]	[Al/Fe]	[Zr/Fe]	[La/Fe]	[Nd/Fe]	[Eu/Fe]	RGB/Field[a]
18174532−3353235	4540	1.45	−1.54	1.65	−0.31	+0.12	+0.44	+0.71	+0.76	+0.93	RGB/1
18182918−3341405	4125	0.95	−1.27	1.60	−0.22	+0.25	+0.02	+0.32	+0.36	+0.48	RGB/1
18175567−3343063	4425	1.30	−1.18	1.15	−0.33	+0.28	−0.02	+0.23	+0.28	+0.27	RGB/1
18181521−3352294	4215	1.00	−1.03	1.55	+0.03	+0.58	+0.68	+0.27	+0.38	+0.26	RGB/1
18182256−3401248	4465	1.10	−1.02	1.15	−0.58	−0.23	+0.07	+0.28	+0.27	+0.21	RGB/1
18174351−3401412	4450	1.35	−0.93	1.25	−0.70	−0.52	−0.02	−0.05	+0.30	+0.29	RGB/1
18172965−3402573	4155	1.35	−0.83	1.80	−0.26	+0.19	+0.33	+0.24	+0.25	+0.22	RGB/1
18183521−3344124	4150	1.25	−0.79	1.85	−0.51	−0.19	−0.05	+0.05	+0.09	+0.28	RGB/1
18181435−3350275	4340	1.20	−0.78	1.25	−0.40	+0.13	+0.15	−0.01	+0.06	+0.21	RGB/1
18183876−3403092	4000	1.05	−0.78	1.80	+0.00	+0.27	+0.28	+0.00	−0.02	+0.32	RGB/1
18174304−3357006	4090	1.00	−0.74	1.45	−0.21	+0.19	+0.37	−0.02	+0.21	+0.18	RGB/1
18180550−3407117	4335	1.25	−0.59	1.45	−0.01	+0.27	−0.09	−0.24	−0.02	+0.03	RGB/1
18180831−3405309	4100	1.00	−0.59	1.95	+0.14	+0.30	−0.14	−0.11	−0.01	+0.30	RGB/1
18174941−3353025	4275	1.40	−0.58	1.95	−0.16	+0.18	−0.04	−0.06	+0.01	+0.27	RGB/1
18174742−3348098	4130	1.45	−0.56	1.45	−0.24	+0.11	+1.11	+1.43	+1.26	+0.50	RGB/1
18183679−3251454	4025	1.10	−0.51	2.00	···	−0.05	···	−0.17	+0.06	+0.00	RGB/2
18181929−3404128	4020	0.90	−0.48	1.30	+0.01	+0.16	+0.26	−0.22	+0.08	+0.20	RGB/1
18183802−3355441	4325	1.25	−0.44	1.75	−0.06	+0.19	−0.15	−0.29	−0.06	+0.20	RGB/1
18181512−3353545	4270	1.45	−0.44	1.65	−0.26	···	−0.05	···	···	···	RGB/1
18174303−3355118	4220	1.30	−0.43	1.60	−0.17	+0.21	+0.11	−0.17	+0.08	+0.42	RGB/1
18182470−3342166	4145	1.10	−0.42	1.60	+0.14	+0.37	−0.09	−0.26	−0.06	+0.21	RGB/1
18180285−3342004	4140	1.30	−0.41	1.45	−0.22	+0.08	−0.10	−0.32	−0.07	+0.30	RGB/1
18174935−3404217	4360	1.25	−0.40	1.70	+0.30	+0.37	+0.14	−0.20	+0.03	−0.01	RGB/1
18174929−3347192	4875	2.35	−0.34	1.40	−0.11	+0.15	+0.06	+0.05	−0.31	+0.28	Clump/1
18183604−3342349	4105	0.80	−0.32	1.90	+0.32	+0.26	−0.08	−0.43	−0.18	+0.11	RGB/1
18173554−3405009	4625	2.10	−0.31	1.60	+0.03	+0.08	−0.11	−0.19	+0.04	+0.00	RGB/1
18180562−3346548	4220	1.30	−0.31	1.75	+0.38	+0.44	+0.06	−0.22	−0.14	+0.18	RGB/1
18173180−3349197	4005	1.15	−0.28	1.25	−0.01	+0.09	−0.05	−0.42	+0.03	+0.29	RGB/1
18181924−3350222	4215	1.35	−0.27	1.55	+0.20	+0.27	−0.11	−0.29	−0.33	+0.11	RGB/1
18175593−3400000	4160	1.20	−0.24	1.40	−0.03	+0.12	−0.04	−0.13	+0.14	+0.11	RGB/1
18182089−3348425	4700	2.15	−0.23	1.45	−0.24	−0.02	−0.27	−0.40	−0.17	+0.02	Clump/1
18175546−3404103	4950	2.40	−0.23	1.40	−0.28	+0.08	−0.05	−0.21	+0.21	+0.17	Clump/1
18174798−3359361	4830	2.30	−0.21	1.75	−0.11	+0.13	−0.04	+0.01	+0.24	+0.28	Clump/1
18182430−3352453	4130	1.05	−0.20	1.40	+0.16	+0.25	−0.03	−0.34	−0.10	−0.01	RGB/1

Table 2—Continued

Star 2MASS	T_{eff} (K)	log g (cgs)	[Fe/H]	V_t (km s^{-1})	[Na/Fe]	[Al/Fe]	[Zr/Fe]	[La/Fe]	[Nd/Fe]	[Eu/Fe]	RGB/Field[a]
18180979−3351416	4350	1.65	−0.20	1.70	−0.10	+0.01	−0.38	−0.26	−0.20	+0.14	RGB/1
18182553−3349465	4660	2.00	−0.17	1.75	−0.01	+0.07	−0.18	−0.12	+0.09	−0.04	Clump/1
18173251−3354539	4565	1.85	−0.17	2.10	+0.46	+0.41	−0.01	−0.14	−0.18	+0.26	RGB/1
18181710−3401088	4940	2.40	−0.17	1.45	+0.28	+0.26	+0.32	+0.27	+0.22	+0.26	Clump/1
18180991−3403206	4345	1.80	−0.14	1.75	+0.14	+0.2	−0.16	+0.01	+0.14	+0.21	RGB/1
18180301−3405313	4040	1.00	−0.12	2.05	+0.32	+0.17	−0.02	−0.33	−0.28	−0.04	RGB/1
18180502−3355071	4715	2.35	−0.10	1.60	−0.04	+0.14	−0.21	+0.22	+0.15	+0.27	Clump/1
18182740−3356447	4690	2.35	−0.09	1.55	−0.41	−0.01	−0.46	···	···	+0.28	Clump/1
18182457−3344533	4530	2.10	−0.08	1.90	+0.15	+0.09	−0.05	−0.22	−0.32	+0.17	Clump/1
18182612−3353431	4860	2.40	−0.07	1.65	+0.24	+0.19	+0.15	+0.20	+0.07	−0.29	Clump/1
18172979−3401118	4860	2.40	−0.02	1.40	+0.02	+0.09	+0.01	−0.33	+0.17	+0.11	Clump/1
18183930−3353425	4200	1.40	+0.01	1.75	+0.33	+0.12	−0.28	−0.37	−0.36	−0.05	RGB/1
18174891−3406031	4805	2.40	+0.05	1.70	−0.07	+0.02	−0.05	−0.01	+0.12	+0.04	Clump/1
18181322−3402227	4740	2.40	+0.06	1.50	+0.04	+0.08	+0.15	−0.05	+0.14	−0.02	Clump/1
18181033−3352390	4900	2.50	+0.17	1.30	−0.06	−0.08	−0.07	+0.02	+0.18	−0.11	Clump/1
18174000−3406266	4565	2.30	+0.19	1.85	+0.15	+0.11	−0.12	−0.12	−0.14	+0.03	Clump/1
18180012−3358096	4090	1.50	+0.20	1.95	+0.21	−0.06	−0.18	−0.33	−0.14	−0.16	RGB/1
18175652−3347050	4185	1.65	+0.22	1.40	−0.22	−0.10	−0.28	−0.28	−0.12	−0.23	RGB/1
18182472−3352044	4070	1.45	+0.23	1.80	+0.40	−0.11	−0.35	−0.48	−0.43	−0.19	RGB/1
18173706−3405569	4405	2.20	+0.25	2.10	+0.56	+0.25	+0.00	−0.15	−0.25	+0.09	Clump/1
18182073−3353250	4500	2.30	+0.26	1.55	−0.19	−0.05	−0.32	−0.28	+0.06	−0.22	Clump/1
18174478−3343290	4785	2.40	+0.26	1.85	+0.46	+0.19	+0.18	−0.12	−0.31	−0.19	Clump/1
18173994−3358331	4085	1.45	+0.26	1.65	+0.44	+0.03	−0.13	−0.53	−0.31	−0.12	RGB/1
18183369−3352038	4585	2.35	+0.27	1.55	−0.26	−0.15	−0.33	+0.01	−0.20	−0.05	Clump/1
18183098−3358070	4570	2.35	+0.29	1.65	+0.37	+0.04	−0.04	−0.29	−0.17	−0.30	Clump/1
18174067−3356000	4540	2.35	+0.33	1.70	+0.40	+0.11	+0.07	−0.26	−0.16	−0.15	Clump/1
18173118−3358318	4355	2.00	+0.45	1.85	+0.19	+0.03	−0.38	···	···	···	Clump/1
18182052−3345251	4505	2.30	+0.47	1.75	+0.04	−0.12	−0.19	−0.40	−0.22	−0.18	Clump/1

[a] "RGB": probable RGB member; "Clump": probable red clump member; '1': Field 1 (l=–1°,b=–8.5°); '2': Field 2 (l=0°,b=–8°); see Johnson et al. (2011) for further details

Table 3. Error Estimation

Star	ΔNa	ΔAl	ΔZr	ΔLa	ΔNd	ΔEu
ΔT_{eff}+100 K						
18174532−3353235	+0.08	+0.08	+0.20	+0.02	+0.04	+0.00
18182918−3341405	+0.08	+0.08	+0.24	+0.01	+0.04	−0.02
18175567−3343063	+0.08	+0.07	+0.21	+0.01	+0.03	−0.02
18181521−3352294	+0.09	+0.09	+0.24	+0.02	+0.04	−0.02
18182256−3401248	+0.08	+0.08	+0.21	+0.01	+0.04	−0.01
18174351−3401412	+0.08	+0.07	+0.21	+0.01	+0.03	−0.02
18172965−3402573	+0.08	+0.07	+0.22	+0.02	+0.04	−0.02
18183521−3344124	+0.08	+0.07	+0.22	+0.02	+0.04	−0.02
18181435−3350275	+0.08	+0.07	+0.21	+0.01	+0.03	−0.03
18183876−3403092	+0.08	+0.07	+0.22	+0.02	+0.04	−0.02
18174304−3357006	+0.09	+0.07	+0.21	+0.01	+0.04	−0.03
18180831−3405309	+0.08	+0.07	+0.21	+0.01	+0.04	−0.02
18180550−3407117	+0.08	+0.07	+0.21	+0.01	+0.03	−0.02
18174941−3353025	+0.08	+0.07	+0.21	+0.01	+0.03	−0.02
18174742−3348098	+0.08	+0.07	+0.17	+0.02	+0.04	−0.02
18183679−3251454	···	+0.07	···	+0.02	+0.04	−0.02
18181929−3404128	+0.07	+0.07	+0.19	+0.02	+0.04	−0.02
18181512−3353545	+0.08	···	+0.21	···	···	···
18183802−3355441	+0.08	+0.07	+0.20	+0.01	+0.03	−0.02
18174303−3355118	+0.08	+0.07	+0.20	+0.01	+0.03	−0.02
18182470−3342166	+0.08	+0.07	+0.19	+0.01	+0.04	−0.02
18180285−3342004	+0.08	+0.06	+0.19	+0.02	+0.04	−0.02
18174935−3404217	+0.07	+0.07	+0.20	+0.01	+0.03	−0.02
18174929−3347192	+0.06	+0.06	+0.17	+0.01	+0.02	−0.02
18183604−3342349	+0.08	+0.07	+0.19	+0.01	+0.04	−0.02
18180562−3346548	+0.07	+0.06	+0.20	+0.01	+0.03	−0.02
18173554−3405009	+0.08	+0.07	+0.18	+0.01	+0.03	−0.02
18173180−3349197	+0.07	+0.06	+0.17	+0.01	+0.04	−0.02
18181924−3350222	+0.07	+0.06	+0.19	+0.01	+0.03	−0.02
18175593−3400000	+0.07	+0.06	+0.17	+0.01	+0.03	−0.02

Table 3—Continued

Star	ΔNa	ΔAl	ΔZr	ΔLa	ΔNd	ΔEu
18182089−3348425	+0.07	+0.07	+0.18	+0.01	+0.03	−0.02
18175546−3404103	+0.07	+0.06	+0.16	+0.01	+0.03	−0.01
18174798−3359361	+0.07	+0.06	+0.17	+0.01	+0.03	−0.02
18180979−3351416	+0.07	+0.06	+0.19	+0.01	+0.03	−0.02
18182430−3352453	+0.07	+0.06	+0.17	+0.01	+0.04	−0.02
18173251−3354539	+0.08	+0.07	+0.18	+0.01	+0.03	−0.02
18181710−3401088	+0.07	+0.06	+0.17	+0.01	+0.02	−0.01
18182553−3349465	+0.07	+0.07	+0.18	+0.01	+0.03	−0.02
18180991−3403206	+0.07	+0.06	+0.18	+0.01	+0.04	−0.02
18180301−3405313	+0.07	+0.06	+0.16	+0.01	+0.03	−0.02
18180502−3355071	+0.08	+0.07	+0.17	+0.01	+0.03	−0.01
18182740−3356447	+0.07	+0.07	+0.17	···	···	−0.02
18182457−3344533	+0.08	+0.07	+0.18	+0.01	+0.03	−0.02
18182612−3353431	+0.07	+0.06	+0.16	+0.01	+0.03	−0.01
18172979−3401118	+0.07	+0.06	+0.17	+0.01	+0.03	−0.02
18183930−3353425	+0.06	+0.05	+0.17	+0.01	+0.03	−0.02
18174891−3406031	+0.07	+0.07	+0.17	+0.01	+0.03	−0.02
18181322−3402227	+0.08	+0.07	+0.17	+0.01	+0.03	−0.01
18181033−3352390	+0.07	+0.06	+0.16	+0.01	+0.03	−0.02
18174000−3406266	+0.07	+0.06	+0.17	+0.01	+0.03	−0.02
18180012−3358096	+0.05	+0.04	+0.13	+0.01	+0.03	−0.02
18175652−3347050	+0.05	+0.04	+0.15	+0.02	+0.03	−0.02
18182472−3352044	+0.05	+0.03	+0.14	+0.01	+0.03	−0.02
18173706−3405569	+0.07	+0.05	+0.16	+0.02	+0.04	−0.01
18173994−3358331	+0.04	+0.03	+0.12	+0.01	+0.03	−0.02
18182073−3353250	+0.08	+0.06	+0.17	+0.01	+0.03	−0.02
18174478−3343290	+0.08	+0.07	+0.17	+0.01	+0.03	−0.02
18183369−3352038	+0.08	+0.06	+0.17	+0.02	+0.03	−0.01
18183098−3358070	+0.06	+0.06	+0.17	+0.01	+0.03	−0.02
18174067−3356000	+0.06	+0.06	+0.17	+0.01	+0.03	−0.02
18173118−3358318	+0.05	+0.04	+0.16	···	···	···

Table 3—Continued

Star	ΔNa	ΔAl	ΔZr	ΔLa	ΔNd	ΔEu
18182052−3345251	+0.07	+0.05	+0.17	+0.01	+0.03	−0.02
Δlog(g)+0.3 dex						
18174532−3353235	−0.01	−0.01	−0.03	+0.13	+0.13	+0.13
18182918−3341405	−0.01	+0.00	+0.00	+0.13	+0.13	+0.14
18175567−3343063	−0.01	+0.00	+0.00	+0.13	+0.13	+0.13
18181521−3352294	−0.01	+0.00	+0.01	+0.14	+0.14	+0.15
18182256−3401248	−0.01	−0.01	+0.00	+0.13	+0.13	+0.13
18174351−3401412	−0.01	+0.00	+0.00	+0.13	+0.13	+0.13
18172965−3402573	−0.01	+0.00	+0.02	+0.13	+0.13	+0.13
18183521−3344124	−0.01	+0.00	+0.02	+0.12	+0.12	+0.12
18181435−3350275	−0.01	−0.01	+0.02	+0.12	+0.12	+0.11
18183876−3403092	+0.00	+0.01	+0.03	+0.13	+0.13	+0.13
18174304−3357006	+0.00	+0.01	+0.02	+0.14	+0.14	+0.14
18180831−3405309	+0.01	+0.02	+0.01	+0.14	+0.13	+0.15
18180550−3407117	−0.01	−0.01	+0.02	+0.12	+0.12	+0.12
18174941−3353025	+0.00	+0.00	+0.01	+0.13	+0.13	+0.14
18174742−3348098	+0.00	+0.02	+0.04	+0.14	+0.14	+0.14
18183679−3251454	···	+0.01	···	+0.12	+0.12	+0.12
18181929−3404128	+0.00	+0.01	+0.04	+0.13	+0.13	+0.13
18181512−3353545	+0.00	···	+0.01	···	···	···
18183802−3355441	−0.01	−0.01	+0.02	+0.12	+0.12	+0.12
18174303−3355118	−0.01	+0.00	+0.03	+0.12	+0.12	+0.12
18182470−3342166	+0.00	+0.00	+0.03	+0.12	+0.12	+0.13
18180285−3342004	+0.00	+0.00	+0.03	+0.12	+0.12	+0.12
18174935−3404217	−0.01	−0.01	+0.02	+0.12	+0.12	+0.12
18174929−3347192	+0.00	+0.00	+0.00	+0.14	+0.13	+0.14
18183604−3342349	−0.01	+0.00	+0.03	+0.12	+0.12	+0.12
18180562−3346548	−0.01	+0.01	+0.03	+0.12	+0.12	+0.12
18173554−3405009	+0.00	+0.00	+0.01	+0.13	+0.13	+0.13
18173180−3349197	+0.00	+0.01	+0.05	+0.12	+0.12	+0.11
18181924−3350222	+0.00	+0.01	+0.03	+0.13	+0.13	+0.13

Table 3—Continued

Star	ΔNa	ΔAl	ΔZr	ΔLa	ΔNd	ΔEu
18175593−3400000	−0.01	−0.01	+0.04	+0.11	+0.12	+0.11
18182089−3348425	−0.01	+0.00	+0.01	+0.13	+0.13	+0.12
18175546−3404103	+0.00	+0.00	+0.00	+0.14	+0.14	+0.14
18174798−3359361	+0.00	+0.00	+0.01	+0.13	+0.13	+0.13
18180979−3351416	−0.01	+0.00	+0.02	+0.12	+0.12	+0.12
18182430−3352453	+0.01	+0.03	+0.03	+0.13	+0.13	+0.14
18173251−3354539	+0.00	+0.00	+0.01	+0.13	+0.13	+0.14
18181710−3401088	−0.01	+0.00	+0.00	+0.14	+0.14	+0.14
18182553−3349465	+0.00	+0.01	−0.01	+0.14	+0.14	+0.15
18180991−3403206	−0.01	+0.00	+0.02	+0.12	+0.13	+0.13
18180301−3405313	+0.04	+0.04	+0.04	+0.14	+0.14	+0.15
18180502−3355071	+0.00	+0.00	+0.00	+0.13	+0.13	+0.14
18182740−3356447	+0.00	+0.00	+0.00	···	···	+0.13
18182457−3344533	+0.00	+0.00	+0.01	+0.13	+0.13	+0.13
18182612−3353431	+0.00	+0.00	+0.00	+0.14	+0.14	+0.14
18172979−3401118	+0.00	+0.00	+0.00	+0.14	+0.14	+0.14
18183930−3353425	+0.01	+0.02	+0.03	+0.13	+0.13	+0.14
18174891−3406031	+0.00	+0.00	+0.00	+0.14	+0.13	+0.14
18181322−3402227	+0.00	+0.00	+0.00	+0.14	+0.13	+0.14
18181033−3352390	+0.00	+0.00	−0.02	+0.14	+0.14	+0.15
18174000−3406266	−0.01	+0.00	+0.01	+0.13	+0.12	+0.13
18180012−3358096	+0.04	+0.05	+0.05	+0.14	+0.14	+0.15
18175652−3347050	+0.00	+0.02	+0.04	+0.12	+0.12	+0.12
18182472−3352044	+0.02	+0.04	+0.05	+0.14	+0.13	+0.14
18173706−3405569	−0.02	+0.00	+0.03	+0.12	+0.12	+0.11
18173994−3358331	+0.02	+0.04	+0.05	+0.14	+0.14	+0.14
18182073−3353250	+0.00	+0.00	+0.02	+0.13	+0.12	+0.13
18174478−3343290	+0.00	+0.01	+0.00	+0.14	+0.13	+0.14
18183369−3352038	−0.01	+0.01	+0.01	+0.13	+0.13	+0.13
18183098−3358070	−0.01	+0.01	+0.02	+0.13	+0.13	+0.13
18174067−3356000	−0.01	+0.01	+0.02	+0.13	+0.13	+0.13

Table 3—Continued

Star	ΔNa	ΔAl	ΔZr	ΔLa	ΔNd	ΔEu
18173118−3358318	+0.02	+0.04	+0.03	···	···	···
18182052−3345251	−0.01	+0.01	+0.03	+0.12	+0.12	+0.13
Δ[M/H]+0.3 dex						
18174532−3353235	−0.02	−0.02	−0.04	+0.11	+0.11	+0.11
18182918−3341405	−0.01	−0.01	+0.01	+0.11	+0.11	+0.10
18175567−3343063	−0.01	−0.01	−0.02	+0.12	+0.12	+0.11
18181521−3352294	−0.01	−0.01	−0.01	+0.12	+0.12	+0.12
18182256−3401248	−0.02	−0.01	−0.03	+0.11	+0.12	+0.11
18174351−3401412	−0.01	−0.01	−0.02	+0.12	+0.12	+0.11
18172965−3402573	+0.00	+0.00	+0.01	+0.11	+0.12	+0.11
18183521−3344124	+0.00	+0.00	+0.03	+0.11	+0.11	+0.10
18181435−3350275	+0.00	−0.01	+0.00	+0.11	+0.12	+0.10
18183876−3403092	−0.01	+0.00	+0.05	+0.11	+0.12	+0.10
18174304−3357006	+0.00	−0.01	+0.03	+0.11	+0.11	+0.10
18180831−3405309	+0.00	+0.00	+0.04	+0.12	+0.12	+0.11
18180550−3407117	−0.01	+0.00	+0.00	+0.12	+0.12	+0.12
18174941−3353025	+0.00	+0.00	+0.01	+0.12	+0.12	+0.12
18174742−3348098	+0.01	+0.02	+0.06	+0.12	+0.13	+0.12
18183679−3251454	···	+0.02	···	+0.13	+0.13	+0.12
18181929−3404128	+0.01	+0.02	+0.07	+0.12	+0.13	+0.12
18181512−3353545	+0.00	···	+0.02	···	···	···
18183802−3355441	+0.00	−0.01	+0.01	+0.12	+0.12	+0.11
18174303−3355118	+0.00	+0.00	+0.03	+0.12	+0.12	+0.11
18182470−3342166	+0.00	+0.00	+0.04	+0.12	+0.12	+0.11
18180285−3342004	+0.00	+0.00	+0.05	+0.12	+0.12	+0.11
18174935−3404217	−0.02	−0.02	+0.01	+0.11	+0.12	+0.11
18174929−3347192	+0.01	+0.00	+0.01	+0.12	+0.12	+0.11
18183604−3342349	−0.02	−0.02	+0.05	+0.11	+0.12	+0.09
18180562−3346548	−0.03	−0.03	+0.04	+0.11	+0.12	+0.10
18173554−3405009	+0.00	−0.01	+0.02	+0.12	+0.12	+0.11
18173180−3349197	+0.00	+0.00	+0.08	+0.11	+0.12	+0.09

Table 3—Continued

Star	ΔNa	ΔAl	ΔZr	ΔLa	ΔNd	ΔEu
18181924−3350222	−0.02	−0.02	+0.04	+0.11	+0.12	+0.09
18175593−3400000	−0.01	−0.01	+0.05	+0.11	+0.12	+0.09
18182089−3348425	+0.01	+0.00	+0.02	+0.12	+0.13	+0.11
18175546−3404103	+0.02	+0.00	+0.03	+0.12	+0.13	+0.11
18174798−3359361	+0.01	+0.00	+0.02	+0.12	+0.13	+0.11
18180979−3351416	−0.01	−0.01	+0.03	+0.12	+0.12	+0.10
18182430−3352453	−0.01	−0.02	+0.05	+0.11	+0.12	+0.10
18173251−3354539	−0.01	−0.02	+0.02	+0.12	+0.13	+0.11
18181710−3401088	+0.00	+0.00	+0.02	+0.12	+0.13	+0.11
18182553−3349465	+0.00	+0.00	+0.02	+0.12	+0.13	+0.11
18180991−3403206	−0.01	−0.01	+0.04	+0.12	+0.12	+0.11
18180301−3405313	+0.00	−0.01	+0.08	+0.12	+0.13	+0.10
18180502−3355071	+0.00	+0.00	+0.02	+0.12	+0.13	+0.11
18182740−3356447	+0.01	+0.00	+0.02	···	···	+0.11
18182457−3344533	+0.00	−0.01	+0.02	+0.12	+0.13	+0.11
18182612−3353431	−0.01	+0.00	+0.02	+0.13	+0.13	+0.12
18172979−3401118	+0.01	+0.00	+0.01	+0.13	+0.13	+0.12
18183930−3353425	+0.00	+0.01	+0.06	+0.13	+0.13	+0.12
18174891−3406031	+0.01	+0.01	+0.02	+0.13	+0.13	+0.12
18181322−3402227	+0.00	+0.00	+0.01	+0.13	+0.13	+0.12
18181033−3352390	+0.00	+0.00	+0.02	+0.13	+0.13	+0.12
18174000−3406266	−0.01	+0.01	+0.04	+0.13	+0.13	+0.12
18180012−3358096	+0.02	+0.02	+0.07	+0.11	+0.12	+0.10
18175652−3347050	+0.01	+0.01	+0.06	+0.10	+0.11	+0.09
18182472−3352044	+0.02	+0.02	+0.07	+0.10	+0.10	+0.09
18173706−3405569	+0.01	+0.01	+0.04	+0.09	+0.09	+0.08
18173994−3358331	+0.02	+0.01	+0.06	+0.08	+0.09	+0.07
18182073−3353250	+0.01	+0.00	+0.03	+0.08	+0.08	+0.08
18174478−3343290	+0.00	+0.00	+0.01	+0.08	+0.08	+0.08
18183369−3352038	+0.00	+0.00	+0.02	+0.08	+0.08	+0.07
18183098−3358070	+0.00	+0.00	+0.02	+0.07	+0.07	+0.06

Table 3—Continued

Star	ΔNa	ΔAl	ΔZr	ΔLa	ΔNd	ΔEu
18174067−3356000	+0.00	+0.00	+0.02	+0.05	+0.05	+0.05
18173118−3358318	−0.01	+0.00	+0.00	···	···	···
18182052−3345251	+0.00	+0.00	+0.00	−0.01	−0.01	−0.01
ΔV_t+0.3 km s^{-1}						
18174532−3353235	+0.00	+0.00	+0.00	−0.03	−0.02	−0.04
18182918−3341405	−0.01	−0.02	−0.02	−0.04	−0.02	−0.02
18175567−3343063	+0.00	−0.02	−0.01	−0.03	−0.02	−0.02
18181521−3352294	−0.02	−0.05	−0.08	−0.04	−0.03	−0.02
18182256−3401248	−0.01	−0.01	−0.01	−0.05	−0.03	−0.03
18174351−3401412	+0.00	−0.01	−0.01	−0.02	−0.02	−0.03
18172965−3402573	−0.02	−0.04	−0.08	−0.03	−0.02	−0.01
18183521−3344124	−0.01	−0.02	−0.04	−0.02	−0.01	−0.02
18181435−3350275	−0.01	−0.03	−0.04	−0.03	−0.02	−0.03
18183876−3403092	−0.04	−0.05	−0.13	−0.03	−0.01	−0.03
18174304−3357006	−0.03	−0.06	−0.15	−0.04	−0.04	−0.03
18180831−3405309	−0.06	−0.07	−0.05	−0.02	−0.02	−0.03
18180550−3407117	−0.04	−0.05	−0.03	−0.02	−0.02	−0.02
18174941−3353025	−0.03	−0.05	−0.03	−0.02	−0.01	−0.02
18174742−3348098	−0.04	−0.05	−0.31	−0.25	−0.18	−0.05
18183679−3251454	···	−0.05	···	−0.02	−0.02	−0.02
18181929−3404128	−0.08	−0.09	−0.22	−0.04	−0.05	−0.05
18181512−3353545	−0.03	···	−0.05	···	···	···
18183802−3355441	−0.04	−0.06	−0.03	−0.02	−0.01	−0.03
18174303−3355118	−0.05	−0.08	−0.09	−0.03	−0.02	−0.05
18182470−3342166	−0.09	−0.10	−0.08	−0.03	−0.02	−0.04
18180285−3342004	−0.05	−0.08	−0.09	−0.02	−0.02	−0.05
18174935−3404217	−0.09	−0.09	−0.06	−0.02	−0.02	−0.02
18174929−3347192	−0.02	−0.03	−0.01	−0.02	−0.01	−0.02
18183604−3342349	−0.11	−0.09	−0.09	−0.02	−0.02	−0.04
18180562−3346548	−0.12	−0.11	−0.09	−0.02	−0.01	−0.03
18173554−3405009	−0.04	−0.05	−0.01	−0.01	−0.01	−0.01

Table 3—Continued

Star	ΔNa	ΔAl	ΔZr	ΔLa	ΔNd	ΔEu
18173180−3349197	−0.10	−0.10	−0.21	−0.03	−0.05	−0.06
18181924−3350222	−0.10	−0.10	−0.08	−0.02	−0.01	−0.04
18175593−3400000	−0.09	−0.09	−0.13	−0.05	−0.05	−0.04
18182089−3348425	−0.03	−0.04	−0.01	−0.01	−0.01	−0.02
18175546−3404103	−0.01	−0.04	+0.00	−0.01	−0.01	−0.02
18174798−3359361	−0.03	−0.04	−0.01	−0.02	−0.01	−0.02
18180979−3351416	−0.06	−0.06	−0.03	−0.02	−0.01	−0.03
18182430−3352453	−0.11	−0.11	−0.16	−0.04	−0.04	−0.04
18173251−3354539	−0.09	−0.08	−0.02	−0.01	−0.01	−0.02
18181710−3401088	−0.06	−0.05	−0.01	−0.03	−0.01	−0.03
18182553−3349465	−0.05	−0.05	−0.01	−0.02	−0.01	−0.01
18180991−3403206	−0.09	−0.09	−0.05	−0.03	−0.02	−0.03
18180301−3405313	−0.13	−0.10	−0.15	−0.02	−0.02	−0.02
18180502−3355071	−0.05	−0.06	−0.01	−0.03	−0.01	−0.03
18182740−3356447	−0.02	−0.05	−0.01	···	···	−0.03
18182457−3344533	−0.08	−0.07	−0.03	−0.01	+0.00	−0.02
18182612−3353431	−0.07	−0.06	−0.01	−0.03	−0.01	+0.00
18172979−3401118	−0.05	−0.06	−0.01	−0.01	−0.01	−0.02
18183930−3353425	−0.14	−0.11	−0.08	−0.02	−0.01	−0.03
18174891−3406031	−0.05	−0.05	−0.01	−0.02	−0.01	−0.02
18181322−3402227	−0.07	−0.07	−0.03	−0.02	−0.02	−0.02
18181033−3352390	−0.06	−0.05	−0.02	−0.03	−0.02	−0.02
18174000−3406266	−0.11	−0.09	−0.04	−0.02	−0.01	−0.02
18180012−3358096	−0.16	−0.11	−0.15	−0.02	−0.02	−0.02
18175652−3347050	−0.11	−0.11	−0.15	−0.04	−0.03	−0.02
18182472−3352044	−0.18	−0.11	−0.13	−0.02	−0.01	−0.02
18173706−3405569	−0.16	−0.12	−0.08	−0.02	−0.01	−0.02
18173994−3358331	−0.19	−0.14	−0.19	−0.02	−0.02	−0.03
18182073−3353250	−0.08	−0.09	−0.05	−0.02	−0.02	−0.01
18174478−3343290	−0.12	−0.08	−0.03	−0.02	+0.00	−0.01
18183369−3352038	−0.07	−0.08	−0.03	−0.03	−0.01	−0.02

Table 3—Continued

Star	ΔNa	ΔAl	ΔZr	ΔLa	ΔNd	ΔEu
18183098−3358070	−0.14	−0.10	−0.06	−0.02	−0.01	−0.01
18174067−3356000	−0.15	−0.11	−0.08	−0.02	−0.01	−0.02
18173118−3358318	−0.17	−0.13	−0.07	···	···	···
18182052−3345251	−0.13	−0.10	−0.07	−0.01	−0.01	−0.02
Line–to–Line Dispersion[a]						
18174532−3353235	0.10	0.10	0.10	0.07	0.07	0.07
18182918−3341405	0.02	0.04	0.07	0.07	0.07	0.07
18175567−3343063	0.04	0.10	0.10	0.07	0.07	0.07
18181521−3352294	0.02	0.04	0.06	0.07	0.07	0.07
18182256−3401248	0.00	0.07	0.14	0.07	0.07	0.07
18174351−3401412	0.04	0.10	0.00	0.07	0.07	0.07
18172965−3402573	0.01	0.11	0.00	0.07	0.07	0.07
18183521−3344124	0.10	0.04	0.12	0.07	0.07	0.07
18181435−3350275	0.00	0.10	0.09	0.07	0.07	0.07
18183876−3403092	0.04	0.09	0.10	0.07	0.07	0.07
18174304−3357006	0.02	0.10	0.09	0.07	0.07	0.07
18180831−3405309	0.05	0.04	0.04	0.07	0.07	0.07
18180550−3407117	0.10	0.11	0.04	0.07	0.07	0.07
18174941−3353025	0.06	0.14	0.02	0.07	0.07	0.07
18174742−3348098	0.10	0.07	0.28	0.07	0.07	0.07
18183679−3251454	···	0.08	···	0.07	0.07	0.07
18181929−3404128	0.03	0.04	0.04	0.07	0.07	0.07
18181512−3353545	0.14	···	0.02	···	···	···
18183802−3355441	0.07	0.07	0.08	0.07	0.07	0.07
18174303−3355118	0.05	0.04	0.04	0.07	0.07	0.07
18182470−3342166	0.07	0.07	0.01	0.07	0.07	0.07
18180285−3342004	0.01	0.11	0.07	0.07	0.07	0.07
18174935−3404217	0.07	0.05	0.09	0.07	0.07	0.07
18174929−3347192	0.07	0.13	0.11	0.07	0.07	0.07
18183604−3342349	0.10	0.04	0.10	0.07	0.07	0.07
18180562−3346548	0.04	0.07	0.07	0.07	0.07	0.07

Table 3—Continued

Star	ΔNa	ΔAl	ΔZr	ΔLa	ΔNd	ΔEu
18173554−3405009	0.03	0.04	0.09	0.07	0.07	0.07
18173180−3349197	0.10	0.09	0.18	0.07	0.07	0.07
18181924−3350222	0.18	0.07	0.04	0.07	0.07	0.07
18175593−3400000	0.11	0.04	0.04	0.07	0.07	0.07
18182089−3348425	0.09	0.10	0.07	0.07	0.07	0.07
18175546−3404103	0.02	0.07	0.04	0.07	0.07	0.07
18174798−3359361	0.05	0.06	0.21	0.07	0.07	0.07
18180979−3351416	0.00	0.09	0.02	0.07	0.07	0.07
18182430−3352453	0.06	0.07	0.11	0.07	0.07	0.07
18173251−3354539	0.02	0.12	0.11	0.07	0.07	0.07
18181710−3401088	0.08	0.05	0.10	0.07	0.07	0.07
18182553−3349465	0.04	0.14	0.00	0.07	0.07	0.07
18180991−3403206	0.07	0.04	0.07	0.07	0.07	0.07
18180301−3405313	0.00	0.07	0.02	0.07	0.07	0.07
18180502−3355071	0.08	0.19	0.16	0.07	0.07	0.07
18182740−3356447	0.10	0.10	0.10	···	···	0.07
18182457−3344533	0.04	0.01	0.04	0.07	0.07	0.07
18182612−3353431	0.09	0.05	0.11	0.07	0.07	0.07
18172979−3401118	0.00	0.11	0.01	0.07	0.07	0.07
18183930−3353425	0.05	0.11	0.03	0.07	0.07	0.07
18174891−3406031	0.05	0.04	0.00	0.07	0.07	0.07
18181322−3402227	0.03	0.16	0.00	0.07	0.07	0.07
18181033−3352390	0.01	0.06	0.00	0.07	0.07	0.07
18174000−3406266	0.01	0.14	0.03	0.07	0.07	0.07
18180012−3358096	0.01	0.06	0.04	0.07	0.07	0.07
18175652−3347050	0.00	0.18	0.04	0.07	0.07	0.07
18182472−3352044	0.04	0.11	0.03	0.07	0.07	0.07
18173706−3405569	0.06	0.21	0.00	0.07	0.07	0.07
18173994−3358331	0.07	0.06	0.09	0.07	0.07	0.07
18182073−3353250	0.11	0.12	0.06	0.07	0.07	0.07
18174478−3343290	0.04	0.18	0.05	0.07	0.07	0.07

Table 3—Continued

Star	ΔNa	ΔAl	ΔZr	ΔLa	ΔNd	ΔEu
18183369−3352038	0.06	0.16	0.02	0.07	0.07	0.07
18183098−3358070	0.01	0.11	0.00	0.07	0.07	0.07
18174067−3356000	0.08	0.13	0.00	0.07	0.07	0.07
18173118−3358318	0.06	0.04	0.04	···	···	···
18182052−3345251	0.08	0.11	0.02	0.07	0.07	0.07
Total Uncertainty: $(\Sigma\sigma^2)^{0.5}$						
18174532−3353235	0.13	0.13	0.23	0.19	0.19	0.19
18182918−3341405	0.08	0.09	0.25	0.19	0.19	0.19
18175567−3343063	0.09	0.12	0.23	0.19	0.19	0.19
18181521−3352294	0.10	0.11	0.26	0.20	0.20	0.21
18182256−3401248	0.08	0.11	0.26	0.19	0.20	0.19
18174351−3401412	0.09	0.12	0.21	0.19	0.19	0.19
18172965−3402573	0.08	0.13	0.24	0.19	0.20	0.18
18183521−3344124	0.13	0.08	0.26	0.18	0.18	0.17
18181435−3350275	0.08	0.13	0.23	0.18	0.19	0.17
18183876−3403092	0.10	0.13	0.28	0.19	0.19	0.18
18174304−3357006	0.10	0.14	0.28	0.20	0.20	0.19
18180831−3405309	0.11	0.11	0.22	0.20	0.20	0.20
18180550−3407117	0.13	0.14	0.22	0.18	0.19	0.18
18174941−3353025	0.10	0.17	0.21	0.19	0.19	0.20
18174742−3348098	0.13	0.11	0.46	0.32	0.27	0.20
18183679−3251454	···	0.12	···	0.19	0.20	0.18
18181929−3404128	0.11	0.12	0.30	0.20	0.21	0.20
18181512−3353545	0.17	···	0.22	···	···	···
18183802−3355441	0.11	0.12	0.22	0.18	0.19	0.18
18174303−3355118	0.11	0.11	0.23	0.19	0.19	0.18
18182470−3342166	0.14	0.14	0.21	0.19	0.19	0.19
18180285−3342004	0.09	0.15	0.23	0.19	0.19	0.18
18174935−3404217	0.14	0.13	0.23	0.18	0.19	0.18
18174929−3347192	0.10	0.14	0.20	0.20	0.19	0.19
18183604−3342349	0.17	0.12	0.24	0.18	0.19	0.17

Table 3—Continued

Star	ΔNa	ΔAl	ΔZr	ΔLa	ΔNd	ΔEu
18180562−3346548	0.15	0.15	0.24	0.18	0.19	0.17
18173554−3405009	0.09	0.09	0.20	0.19	0.19	0.18
18173180−3349197	0.16	0.15	0.34	0.18	0.19	0.17
18181924−3350222	0.22	0.14	0.22	0.19	0.19	0.18
18175593−3400000	0.16	0.11	0.23	0.18	0.19	0.16
18182089−3348425	0.12	0.13	0.19	0.19	0.20	0.18
18175546−3404103	0.08	0.10	0.17	0.20	0.21	0.19
18174798−3359361	0.09	0.09	0.27	0.19	0.20	0.19
18180979−3351416	0.09	0.13	0.20	0.18	0.19	0.17
18182430−3352453	0.14	0.15	0.26	0.19	0.20	0.19
18173251−3354539	0.12	0.16	0.21	0.19	0.20	0.19
18181710−3401088	0.13	0.09	0.20	0.20	0.20	0.19
18182553−3349465	0.09	0.17	0.18	0.20	0.21	0.20
18180991−3403206	0.13	0.11	0.20	0.19	0.20	0.19
18180301−3405313	0.15	0.14	0.24	0.20	0.21	0.19
18180502−3355071	0.13	0.21	0.23	0.19	0.20	0.19
18182740−3356447	0.12	0.13	0.20	···	···	0.19
18182457−3344533	0.12	0.10	0.19	0.19	0.20	0.19
18182612−3353431	0.14	0.10	0.19	0.21	0.21	0.20
18172979−3401118	0.09	0.14	0.17	0.20	0.21	0.20
18183930−3353425	0.16	0.16	0.20	0.20	0.20	0.20
18174891−3406031	0.10	0.09	0.17	0.20	0.20	0.20
18181322−3402227	0.11	0.18	0.17	0.20	0.20	0.20
18181033−3352390	0.09	0.10	0.16	0.21	0.21	0.21
18174000−3406266	0.13	0.18	0.18	0.20	0.19	0.19
18180012−3358096	0.17	0.14	0.22	0.19	0.20	0.19
18175652−3347050	0.12	0.21	0.23	0.18	0.18	0.17
18182472−3352044	0.19	0.16	0.21	0.19	0.18	0.18
18173706−3405569	0.18	0.25	0.19	0.17	0.17	0.15
18173994−3358331	0.21	0.16	0.26	0.18	0.18	0.17
18182073−3353250	0.16	0.16	0.19	0.17	0.16	0.17

Table 3—Continued

Star	ΔNa	ΔAl	ΔZr	ΔLa	ΔNd	ΔEu
18174478−3343290	0.15	0.21	0.18	0.18	0.17	0.18
18183369−3352038	0.12	0.19	0.18	0.17	0.17	0.16
18183098−3358070	0.15	0.16	0.18	0.16	0.17	0.16
18174067−3356000	0.18	0.18	0.19	0.16	0.16	0.16
18173118−3358318	0.19	0.15	0.18	···	···	···
18182052−3345251	0.17	0.15	0.19	0.14	0.14	0.15

[a]A value of 0.07 dex (the average line–to–line dispersion for all elements where more than one line was measured) was set for elements and/or stars where only a single line was available.